In-depth evaluation of laser-welded similar and dissimilar material tab-to-busbar electrical interconnects for electric vehicle battery pack

Nikhil Kumar[*], Iain Masters, Abhishek Das

WMG, The University of Warwick, Coventry CV4 7AL, UK
*Corresponding author: nikhil.kumar@warwick.ac.uk

Abstract

A recent increase in the use of electric vehicles demands an efficient and faster joining process for making electrical interconnects within the battery pack. The choice of tab and busbar materials to produce those electrical interconnects is mainly based on weldability, weight, electrical/ thermal conductivity and cost. To meet the high joining demand and low cycle time, laser welding is emerging as the main joining technology due to its ability to weld a variety of materials at a high speed. This paper investigates laser overlap welding for producing similar and dissimilar material tab-to-busbar interconnects for Li-ion battery assembly. In this research, 0.3 mm Al, Cu, Cu[Ni] and Ni tabs were welded with 1.5 mm Al and Cu busbars using a 150 W pulsed fibre laser system integrated with a wobble head. The weldability and joint suitability analyses were conducted by evaluating joint strength, joint intermetallic compound (IMC) formation, joint resistance and temperature rise with the aim of developing a better and safer battery system. It was observed that a maximum joint strength of 930 N was obtained from the Ni tab to Al busbar joints which was approximately 109%, 44% and 66% more than the strength obtained for Al, Cu[Ni] and Cu tab to Al busbar joints respectively. In the case of Cu busbar based tab connections, the maximum joint strength (1320N) was obtained from the Ni tab, which is 152%, 71% and 76% more than Al, Cu[Ni], and Cu tab to Cu busbar joint strength respectively. The strength obtained for the Cu tab to Al busbar (about 560 N) was slightly more than the Al tab to Cu busbar (about 520 N) due to the formation of $CuAl_2$ IMCs at the weld interface of Al tab to Cu busbar joints. Weld microstructure studies provided insightful information on under-weld, good-weld and over-weld characterisation with respect to IMC formation and correlated with the joint strength. In addition, electrical resistance and temperature rise at the joint are equally important for electric vehicle battery applications. The change in contact resistance and joint temperature rise was measured simultaneously for 180 s at different amplitudes of current (i.e., 100 A, 150 A and 200 A) passed through the joints.

1. Introduction

Electric vehicles (EVs) Hybrid/Plug-in Hybrid Electric Vehicles (HEVs/PHEVs) have either zero or low tailpipe emissions making them cleaner and better for the environment than traditional fossil fuel-based vehicles by reducing the emission of greenhouse gases [1, 2]. Compared with other battery electrochemistry's (e.g., lead-acid, NiCd and NiMH), Lithium-ion (Li-ion) batteries are the most appropriate for energy storage applications [3] due to their favourable attributes such as longer lifespan, higher densities of energy/power and portability [4]. As a result, Li-ion batteries are extensively used for various applications including cell phones, laptops, digital cameras, other portable electronic devices, and electrical grid storage [4]. In addition, Li-ion battery cells are being extensively used to build battery packs for electric vehicles. Essential to meet the energy demands of the vehicle large numbers of cells must be connected within the battery pack. Pouch cells are one of the common cell formats used by OEMS including Nissan, Chevrolet and Hyundai to build automotive battery packs [5] in which numerous cells must be connected in series/parallel to create battery packs with the necessary voltage and amperage to deliver the required power and driving ranges. Often, this is obtained by connecting the pouch cell tabs with the busbar. Similarly, cylindrical cell-based battery modules, which may contain several thousand individual cells, need connections to the cell terminals and busbar [66]. Suitable joining techniques are therefore required to fulfil the growing demand for electrical vehicles. Overlap welding is generally used to create the battery interconnects between a thin tab and a thick busbar, often made of dissimilar materials, as shown in **Fig. 1**. The joining process must be highly automated to make volume manufacture economic and maintain joint quality.

Several welding techniques have been identified by researchers for automotive battery pack manufacturing e.g., laser beam welding (LBW), resistance spot welding and ultrasonic welding process [5, 56]. Of these LBW is preferred for welding individual battery cells [6-12] due to its advantages of high-power density, small heat-affected zone, high welding speed, reproducibility, flexibility, easy automation and non-contact joining etc. Brand et al. [6], investigated different welding techniques (e.g., resistance spot welding, ultrasonic welding and laser beam welding) for battery cell to tab welding, and studied the electrical contact resistance of the welds produced. They found that the electrical contact resistance for each of the welding techniques varied with the weld area, and that the highest joint strengths and lowest electrical contact resistances were obtained with LBW because the optimal weld geometry could be achieved. LBW was widely adopted for different types of joints such as overlap, butt and T-

joint configurations [28-32, 57, 58]. In order to increase the width of the weld seam between the work materials and to get a stable welding depth, a beam oscillation technique can be applied [7, 8]. The high energy density of the laser source permits high welding speed which can be used to control/limit the energy input into the battery cell [9, 10]. LBW allows flexibility in the joint design which can be used/adapted for various types of battery module and pack joining applications [11]. Similarly, pouch cell tabs and busbars with numerous thicknesses, i.e., varying stack-up, can be welded using LBW. Solchenbach et al. [12] examined the laser beam braze-welding process for dissimilar aluminium–copper interconnects for Li-ion battery cells and found that the contact resistance was less sensitive to the thickness of the intermetallic compounds (IMCs) formed than the mechanical strength. However, the strength and electrical conductivity were significantly reduced by increasing the thickness of intermetallic compounds [13]. In general, during the dissimilar LBW/fusion welding process, materials were mixed and consequently alloyed. As a result, several IMCs were formed which are brittle having high hardness and high specific electrical resistance [12]. Therefore, the IMCs layers must be as thin as possible to provide high joint strength and low electrical contact resistance. The melting phenomenon at the metallic mixed joint, keyhole geometry, weld pool turbulence and solidification behaviour can be influenced by a few key parameters like a high frequent time-, position- and power-controlled laser beam oscillation [14]. Due to the focused energy input and high-power density, LBW allows a controlled heat distribution and a reduced interaction of the joining materials. Thus, the formation of brittle IMCs could be lowered/avoided [15]. Schmitz et al. [16] concluded that a pulsed welding strategy with disconnected weld seams was able to minimize the heat input and provide a high degree of flexibility during the welding of electrical connections for cylindrical lithium-ion batteries. Pulsed LBW proved to be preferable to conventional resistance spot welding in this application since no adverse impact on the electrical properties of the cell could be detected due to the minimum heat input. For conductive materials such as aluminium and copper in battery pack welding applications, the use of single-mode fibre lasers has added advantages such as the ability to focus to a small spot size (~ 30-micron), high welding speed and cost-effective welding solution [17]. For highly reflective and conductive materials, a few researchers have investigated blue laser welding due to a higher absorption rate in comparison with conventional IR laser. For example, Wang et al. [62] studied the development of a high-power blue laser (445 nm) for material processing (i.e., heat treatment and cladding). They have found that the absorption rate of the blue laser system for the steel was 2.75 times that of a single-mode fibre laser system (1070 nm). Furthermore, the rate of absorption increases significantly for highly reflective materials, such as Cu, Ni, or Al

(i.e., the absorption ratio of Blue laser to IR laser are 13X, 1.5X and 3X for Cu, Ni, and Al, respectively) [65]. In addition, Zediker et al. [63], Das et al. [64] and Boese et al. [65] used a blue laser for the application of electric vehicle component welding. They have concluded that the blue laser would be effective in controlling the keyhole formation and depth of penetration as increased stability can be achieved even at a higher welding speed. In addition, blue laser welding resulted in improved quality with low spatter, low welding cracks with little or no porosity within the fusion zone. The obtained results confirmed that a wide range of process parameters can be used to weld dissimilar materials with minimal defects using a blue laser.
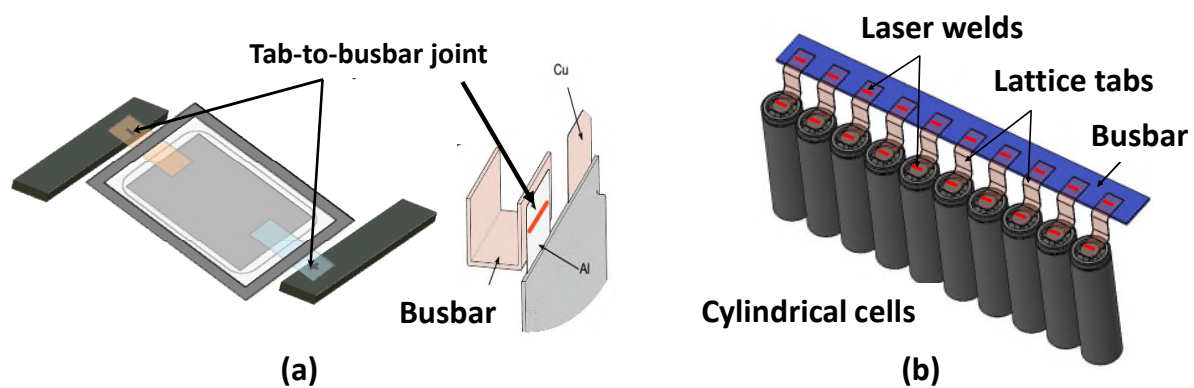

Fig. 1. An illustration of tab-to-busbar joints made during (a) pouch cell-based (b) cylindrical cell-based module manufacture [adapted from 12 and 27]

The key goal of electrical contacts of a high-performance device is the transmission of electrical power with low power dissipation. Schmidt et al. [18] suggested that the electrical resistance can be decreased by applying the LBW process. They optimized (genetic algorithm) the geometrical shape of the weld seam to minimize the resistance of the electrical contact for a battery pack with eight Li-ion cells. The battery tab or lattice tab is the bridge that connects positive and negative cell terminals to the external busbar circuit. Traditionally, the tabs are thin foil made of a single material such as Al, Ni or Cu and sometimes coated with a thin layer of material to improve the corrosion resistance and welding quality, e.g., Cu tabs can be coated with Ni [19]. The selection of busbar material and its thickness are based on the current carrying capacity, mechanical and electrical characteristics and cost of the module [20]. The busbar plays a vital role in avoiding excessive heat generation at the tab-to-busbar interconnects. Copper and aluminium are widely adopted as busbar materials for the automotive industries [11]. Traditionally, copper was used for busbars owing to its outstanding mechanical and

electrical properties. More recently aluminium has been considered, especially for lightweight applications. Only limited information is available for the selection of suitable tab-to-busbar material combinations based on the mechanical strength, electrical resistance and temperature rise at the joint due to current flow during charging and discharging cycles. Das et al [33] evaluated the mechanical strength, electrical resistance and temperature rise in ultrasonically bonded Cu and Al busbar materials of varying thicknesses (i.e., 1.0 mm to 2.5 mm). They concluded that electrical resistance decreased with the increasing thickness of busbars and the average temperature increase from the 0.3 mm Al tab was 0.6 times higher than the 0.3 mm Cu tab, irrespective of busbar selection. Helm et al. [35] studied the influence of the surface properties of the connector material on the reliability and reproducibility of laser beam welded tab to battery cell contacts. They found that the mechanical properties were reduced if copper connector ribbons, in a combined wire bonding laser welding process, were oxidised and subsequently roughened to improve weldability by reducing the surface reflectance.

Within the scope of the literature review, it was observed that the in-depth analysis on intermetallic compound (IMC) formation, electrical contact resistance and joint strength of battery tab-to-busbar welding has not been fully investigated. However, a detailed analysis is needed for laser-welded joints and subsequent selection of tab-to-busbar material combinations. In addition, the temperature rises at the laser-welded joint due to the application of a high charge/discharge current is also necessary to avoid undesired outcomes such as joint failure or thermal runaway. To address this issue, Das et al [26] characterised ultrasonic joints for Li-ion batteries to evaluate the impact on electrical resistance and temperature rise. Similarly, for the laser-welded joint, Shaikh et al [34] conducted electro-thermo-mechanical behaviours considering nickel-plated steel and nickel-plated copper tabs of 0.3 mm thickness. They reported that due to the effect of Joule heating, a rise in joint temperature was obtained when the current was passed through the joint. The range of temperature change was between 72.19 °C to 78.49 °C for 75 A current passed for 120 s. However, the detailed thermal characterisation for the laser-welded joints for various material stack-ups is still missing from the literature. Several aspects need to be explored to develop a sound knowledge base in this area. Taking this into consideration, the present work is planned to develop an in-depth evaluation of laser welding of various combinations of tab-to-busbar electrical interconnects for electric vehicle battery pack applications using a pulsed fibre laser welding process considering beam wobbling techniques. This study will help industries to select a suitable combination of tab and busbar materials for their battery modules.

The main focus of the work:

- To determine the preferred process parameters to achieve the maximum joint strength and minimum contact resistance for numerous combinations of tab-to-busbar joints i.e., aluminium-aluminium (Al-Al), nickel-aluminium (Ni-Al), copper-aluminium (Cu-Al), Cu[Ni]-Al, Al-Cu, Ni-Cu, Cu-Cu and Cu[Ni]-Cu.
- To investigate the joint microstructure, analyse defects and determine the effect of intermetallic compounds (IMCs) on joint strength
- To correlate electrical resistance of various stack-up combinations with the temperature rise at the joint due to the application of charge/discharge current.
- To identify the suitability of the various stack-up material combinations for industrial application in terms of tab and busbar materials selection.

2. Experimental setup and procedure

In this experimental work, the thin tab and thick busbar of dimensions 50 mm $\times$ 15mm $\times$ 0.2 mm and 50 mm $\times$ 15 mm $\times$ 1.5 mm were chosen respectively. Al, Ni, Cu and Cu[Ni] were selected as tab materials whereas Al and Cu as busbar materials because these are highly conductive which is essential for reducing power dissipation [11, 15, 17, 39] and they are commonly used for industrial battery applications. Subsequently, the welding was conducted for all the combinations of tab and busbar materials i.e., Al (tab) - Al (busbar), Ni (tab) - Al (busbar), Cu (tab) - Al (busbar), Cu[Ni] (tab) - Al (busbar), Al (tab) - Cu (busbar), Ni (tab) - Cu (busbar), Cu (tab) - Cu (busbar) and Cu[Ni] (tab) - Cu (busbar). In this study, the thin tab was used as the upper material and welded to a thick busbar in lap joint configuration as shown in **Fig. 2**, and a 2.5 mm radius was used for the weld seam formation. Welding was conducted using a 1.5 kW YLR fibre laser in peak power mode (make: IPG Photonics; model: Micro-Multi-axis Laser Processing Workcell) considering wobbling with a constant parameter set as tabulated in **Table 1**. The experiments were performed at different levels of laser power whilst welding speed, pulse on time, wobble frequency and wobble amplitude were kept fixed. Because laser power must be controlled to prevent overheating during welding [21]. Das et al. [36] also found the laser power has the most significant effect on the two key geometric features of the fusion zone, i.e., weld width and penetration depth when laser welding using wobble technique. The limits of laser power were selected based on experimental trials. A clamping device was used to maintain intimate contact between two sheets. An argon gas jet emerging

from a nozzle coaxial with the laser beam was used to avoid any external atmospheric contamination during welding. The chemical compositions of workpieces were given in **Table 2**. **Table 3** presented the electrical and mechanical properties of the tab and busbar materials with their volumetric weight and cost. The fixed process parameters and varied laser power values are presented in **Table 4**.

Table 1. Constant parameters set used in this study

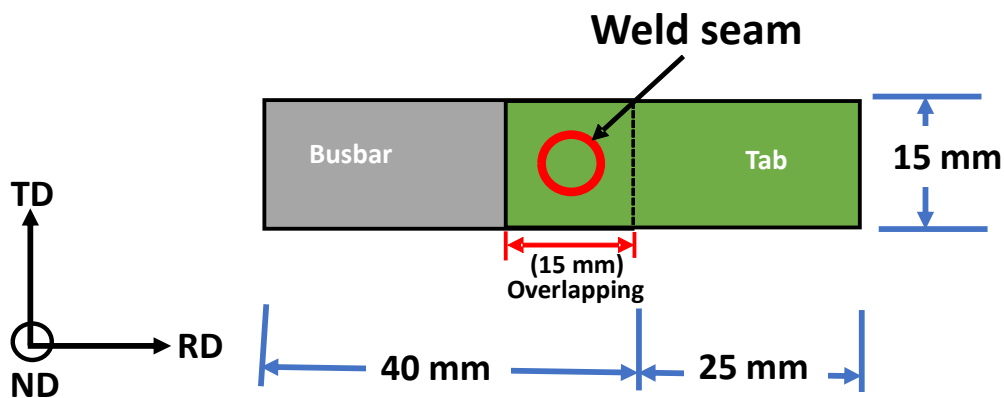| Parameter	Value/Type	Unit
Focus distance	200	mm
Stand-off distance	20-23	mm
Focus position	Top surface	-
Spot size	28	µm
Shield gas	Argon	-
Shield gas flow rate	20	l/min
Wobble mode	Circle Clockwise	-
Wave	Pulsed	

Fig. 2. Joint configuration

Table 2. Chemical composition (wt%) of tab and busbar materials

| Materials		Thickness (mm)	Chemical compositions (wt%)
Upper material - tab	Al	0.3	Si < 0.25, Fe < 0.40, Cu < 0.05, Mn < 0.05, Mg < 0.05, Zn < 0.07, Ti < 0.05, Al balance 99.50, Others 0.03
	Cu	0.3	Cu > 99.99, O < 0.0005, other balance
	Cu[Ni]	0.3	Ni < 10, Fe < 1, Mn < 0.50, Cu Rem.
	Ni	0.3	Ni > 99, Mn < 0.35, Cu < 0.25, Si < 0.35, C < 0.15, S < 0.01, Fe < 0.40, other balance
Lower material - busbar	Al	1.5	Si < 0.25, Fe < 0.40, Cu < 0.05, Mn < 0.05, Mg < 0.05, Zn < 0.07, Ti < 0.05, Al balance 99.50, Others 0.03
	Cu	1.5	Cu > 99.99, O < 0.0005, other balance

Table 3. Electrical and mechanical properties of tabs and busbar materials and their volumetric weight and cost [69, 70]

Materials		Electrical properties	Mechanical properties	Volumetric weight (Kg/m³)	Cost (US$ / ton) [69]
Upper material - tab	Al	$\rho = 2.8 \times 10^{-8}$ Ω.m	TS= 90 MPa, YS= 75 MPa, SS= 70 MPa, λ= 229 W/m.K, MT= 645ºC, α= 24×10⁻⁶ °C⁻¹	2700	2,490.0
	Cu	$\rho = 1.7 \times 10^{-8}$ Ω.m	TS= 210 MPa, λ= 391.1 W/m.K, MT= 1083ºC, α= 16×10⁻⁶ °C⁻¹	8960	10,029.0
	Cu[Ni]	$\rho = 1.9 \times 10^{-8}$ Ω.m	TS= 257 MPa; λ= 354.23 W/m.K MT= 1110ºC	8900	11,235.0
	Ni	$\rho = 7 \times 10^{-8}$ Ω.m	TS= 462 MPa; YS= 148 MPa, λ= 70.2 W/m.K, MT = 1435 ºC	8902	18,303.0
Lower material - busbar	Al	$\rho = 2.8 \times 10^{-8}$ Ω.m	TS= 90 MPa, YS= 75 MPa, SS= 70 MPa, λ= 229 W/m.K, MT= 64 ºC, α= 24×10⁻⁶ °C⁻¹	2700	2,490.0
	Cu	$\rho = 1.71 \times 10^{-8}$ Ω.m	TS= 210 MPa, λ= 391.1 W/m.K, MT= 1083ºC, α= 16×10⁻⁶ °C⁻¹	8960	10,029.0

Note: ρ= Electric resistivity, TS= Tensile strength, YS= Yield strength, SS= Shear strength, λ= thermal conductivity, MT= Melting temperature, α= Coefficient of thermal expansion

Table 4. Process parameters for the tab to busbar joints

Materials		Fixed process parameters	Laser power (W)
Upper material	Lower material		
Al tab	Al busbar	Welding speed= 1000 mm/min Pulse on time = 2 ms Pulse frequency= 100 Hz Wobble amplitude= 0.3 mm Wobble frequency= 600 Hz	300, 375, 450, 525, 600, 675
Cu tab			525, 600, 675, 750, 825, 900, 975, 1050, 1125
Cu[Ni] tab			525, 570, 600, 675, 750, 825, 900
Ni tab			450, 525, 600 750, 825, 900, 975, 1050, 1125
Al tab	Cu busbar		300, 375, 450, 525, 600, 675, 750, 825
Cu tab			525, 600, 675, 750, 825, 900, 975, 1050, 1125, 1200, 1275, 1350
Cu[Ni] tab			525, 600, 675, 750, 825, 900, 975, 1050, 1125, 1200, 1275
Ni tab			675, 750, 825, 900, 975, 1050, 1125, 1200, 1275
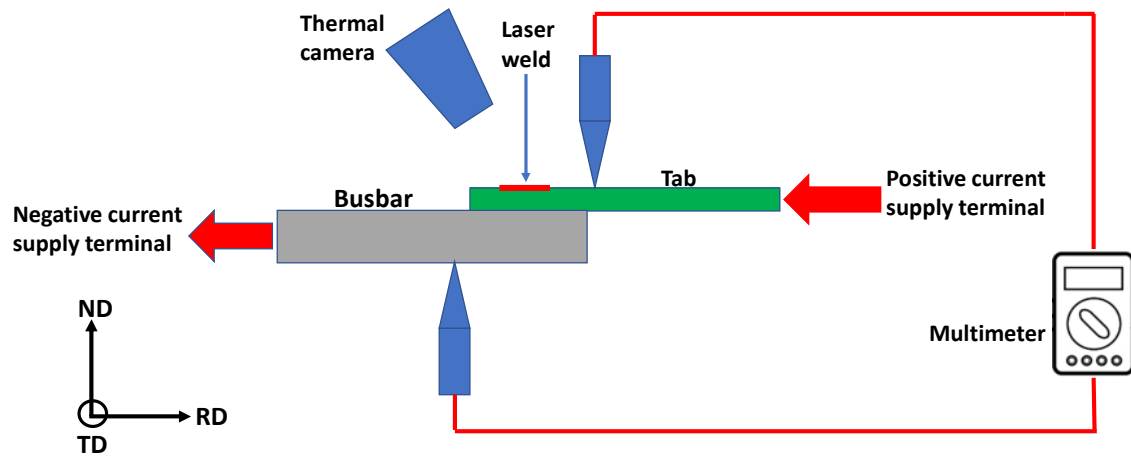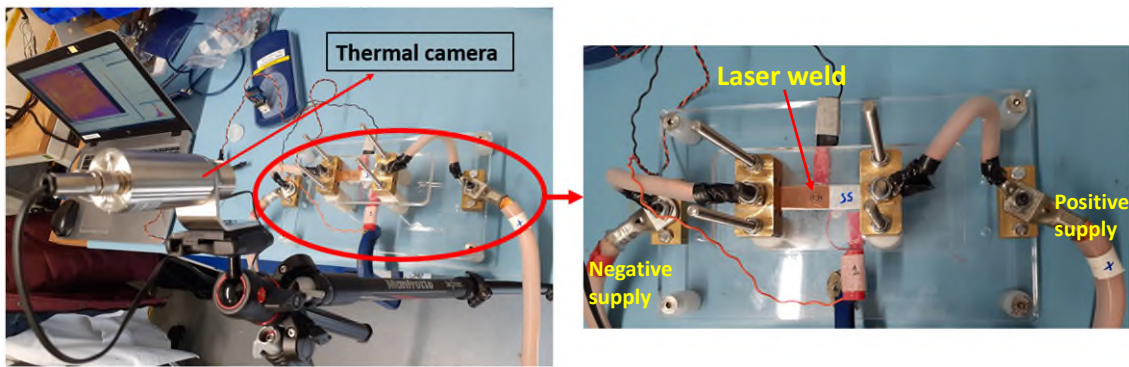
Fig. 3. Resistance and temperature rise measurement (a) schematic diagram and (b) actual experimental set-up

Each experimental combination was replicated three times to get repeatable results and associated standard deviation. The welded samples for Metallographic analysis were sectioned perpendicular to the welding direction. In order to maintain consistency with the terminology typically used for the laser welding process, the principal directions of the laser welding geometry are referred to as RD (rolling direction), ND (normal direction) and TD (transverse direction) respectively. The macrographs were acquired from the ND-RD sections of the weld metal. Samples for the metallographic analysis were prepared by polishing with successively finer SiC papers, down to 1200 grade, to remove the scratches. Each sample was then polished on 3 µm, 1 µm and 0.05 µm diamond solutions. Measurement of the tensile strength of welded samples was conducted on an Instron 3367 test frame with a crosshead speed of 0.5 mm/min and the weld bead geometry was analysed using an optical microscope (Nikon Eclipse LV150N). For electrical contact resistance measurement, the four-wire Kelvin method was used [11]. Field emission scanning electron microscope (FE-SEM) equipped with an energy

dispersive X-Ray analysis (EDX) system was used for microstructural analysis. For measurement of the resistance of the welded specimens, the four-point probe measurement technique [16, 22, 57] was applied in order to reach a high level of accuracy. In general, researchers are using a micro-ohmmeter with four terminals for precise measurement of electrical resistance at milli or micro ohm level. For example, Hu et al. [58] used the same techniques for measuring the contact resistance of the faying surface of the resistance spot welding (RSW) process. Similarly, Brand al. [67] and Solchenbach et al. [68] also used the four-point probes method for calculating the electrical resistance of the welded joints. In the present work, the same method was adopted to measure the electrical contact resistance and corresponding temperature rise. Electrical current was passed through the welded tab and busbar and the voltage drop was measured across the weld as shown in **Fig. 3(a)**. Resistance was calculated by application of Ohm's law (V= IR), from the induced voltage due to application of the current. When the current was supplied, resistive heat loss (I^2R_{weld}) increased the temperature at the welded location. To measure the rise in temperature a thermal camera was used. The schematic and the actual configuration of the testing setup are given in **Fig. 3(a)** and **(b)** respectively. The increase in temperature at the weld was essential to evaluate because of safety and the other end of the tab would be connected to the battery cells casing (contained electrochemically active material) where this temperature-sensitive materials inside the cell limit the maximum heat input (**Fig. 1**). Therefore, a thermal camera (make: Optris PIX Connect) was fixed on the top and focused on the weld during the resistance measurement displayed in **Fig. 3**. A rigid fixture was used to ensure an identical positioning of the voltage measuring pins between the separate experiments.

3.   Results and discussions

The following section details the analysis of laser-welded samples in terms of joint strength, intermetallic formation, contact resistance and increase in temperature. The welded joints were prepared under varying levels of laser power considering three repetitions **(Table 4)**. Examples of a few laser-welded tab (Al, Cu[Ni], Cu and Ni) to Al and Cu busbar samples are shown in **Figures 4** and **5** respectively.
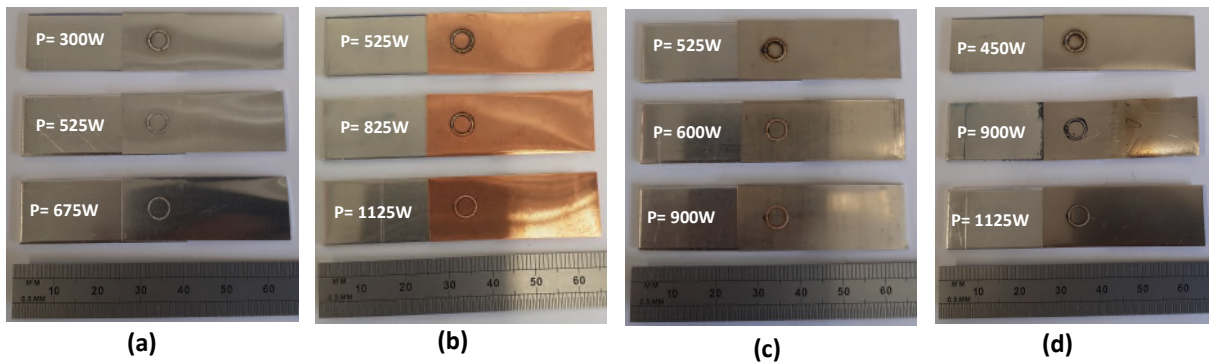
Fig. 4. Laser welded (a) 0.3 mm Al tab to 1.5 mm Al busbar (b) 0.3 mm Cu tab to 1.5 mm Al busbar (c) 0.3 mm Cu[Ni] tab to 1.5 mm Al busbar (a) 0.3 mm Ni tab to 1.5 mm Al busbar
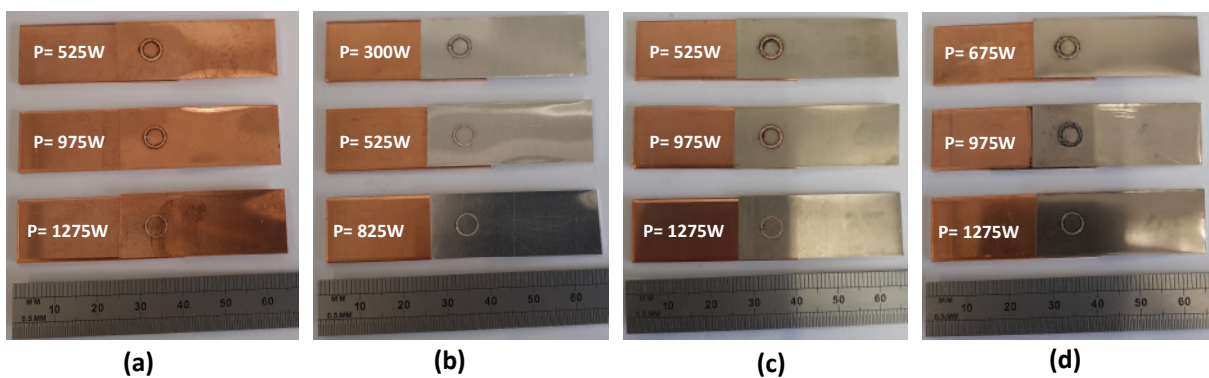

Fig. 5. Laser welded (a) 0.3 mm Cu tab to 1.5 mm Cu busbar (b) 0.3 mm Al tab to 1.5 mm Cu busbar (c) 0.3 mm Cu[Ni] tab to 1.5 mm Cu busbar (a) 0.3 mm Ni tab to 1.5 mm Cu busbar

3.1. Joint strength analysis

3.1.1. Various tabs to Al busbar joint

Joint strength is one of the most important parameters to categorize a weld as good or bad. Lap shear tests were conducted to determine the weld/joint strength. The weld strength was defined in terms of the maximum load which was obtained from the lap shear test on standard width (15 mm) specimens. Hence, the average maximum load (AML) vs the laser power were plotted for the various tab (Al, Cu[Ni], Cu and Ni) to Al busbar joints in **Fig. 6**. From **Fig. 6(a)** to **(c)**, it can be observed that the AML increased with laser power up to a threshold value and thereafter it started to decrease. This can be explained by the bead geometry (i.e., weld pool). When the laser power is low (below the threshold) there is insufficient laser penetration producing an 'under weld' with low joint strength. High joint strengths were obtained above the threshold value of the laser power (i.e., good weld). However, when the laser power was

very high excessive base material melting occurred which caused underfilling and burn-through due to the deeper penetration of the keyhole into the material, and consequently less AML was achieved [23], this corresponds to an 'over weld condition'. In the work of Shaikh et al [34], the weld categories were defined in terms of the penetration depth for Hilumin to copper laser welding. 'Under-weld' corresponded to a penetration depth of less than 0.3 times of thinnest/tab material thickness and 'over-weld' when more than 0.8 times of lower material or full penetration was obtained. Between these limits, defined the region in which a 'good-weld' could be achieved. From **Fig. 6(a)**, the Al tab to Al busbar combination produced a low joint strength of ~300 N at a laser power of 300 W. With the incremental increase in laser power, the joint became better and resulted in a higher load. At the laser power level of 450 W and 525 W, the maximum joint strength of ~450 N was measured. Further increase in laser power reduced the joint strength due to over-weld conditions. Similarly, the effective values of the laser power for producing the good weld, in terms of joint strength, for the various tab materials to aluminium busbar combinations can be determined from **Fig. 6**.
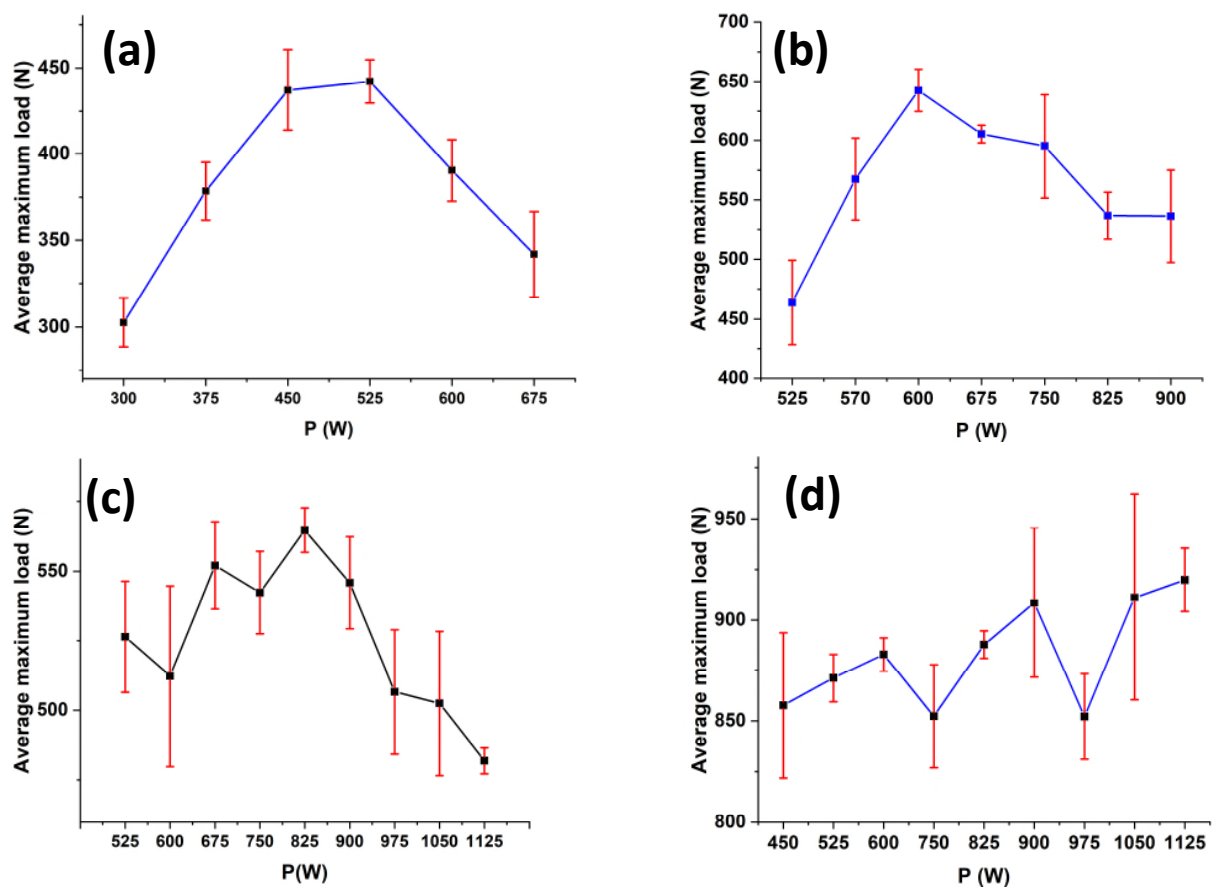

Fig. 6. Average maximum load of laser lap welded 0.3 mm (a) Al (b) Cu[Ni] (c) Cu and (d) Ni tabs to 1.5 mm Al busbar

Ni tab to Al busbar **Fig. 6(d)**, an inconsistent but generally increasing trend was obtained between the laser power and the AML, and a minimum joint strength of ~860 N was obtained at 450 W laser power whereas, the maximum joint strength of ~930 N was obtained at 900 W, 1050 W and 1125 W laser power. The range of parametric conditions for the 'good weld' can also be determined based on joint strength analysis. For example, Al, Cu[Ni], Cu and Ni tabs to Al busbar joints, laser powers of (450 – 525 W), (600 – 675 W), (675 - 900 W) and (825 - 900 W) were required for producing good welds, respectively.

3.1.2. Various Tabs to Cu busbar joint

Fig. 7 shows the laser power vs AML plots for the various tabs to the Cu busbar joint. From **Fig. 7(a)** to **(c)**, a significant increase in AML was obtained for the initial two to three levels of laser power, thereafter insignificant changes were observed within the working limit of laser power.
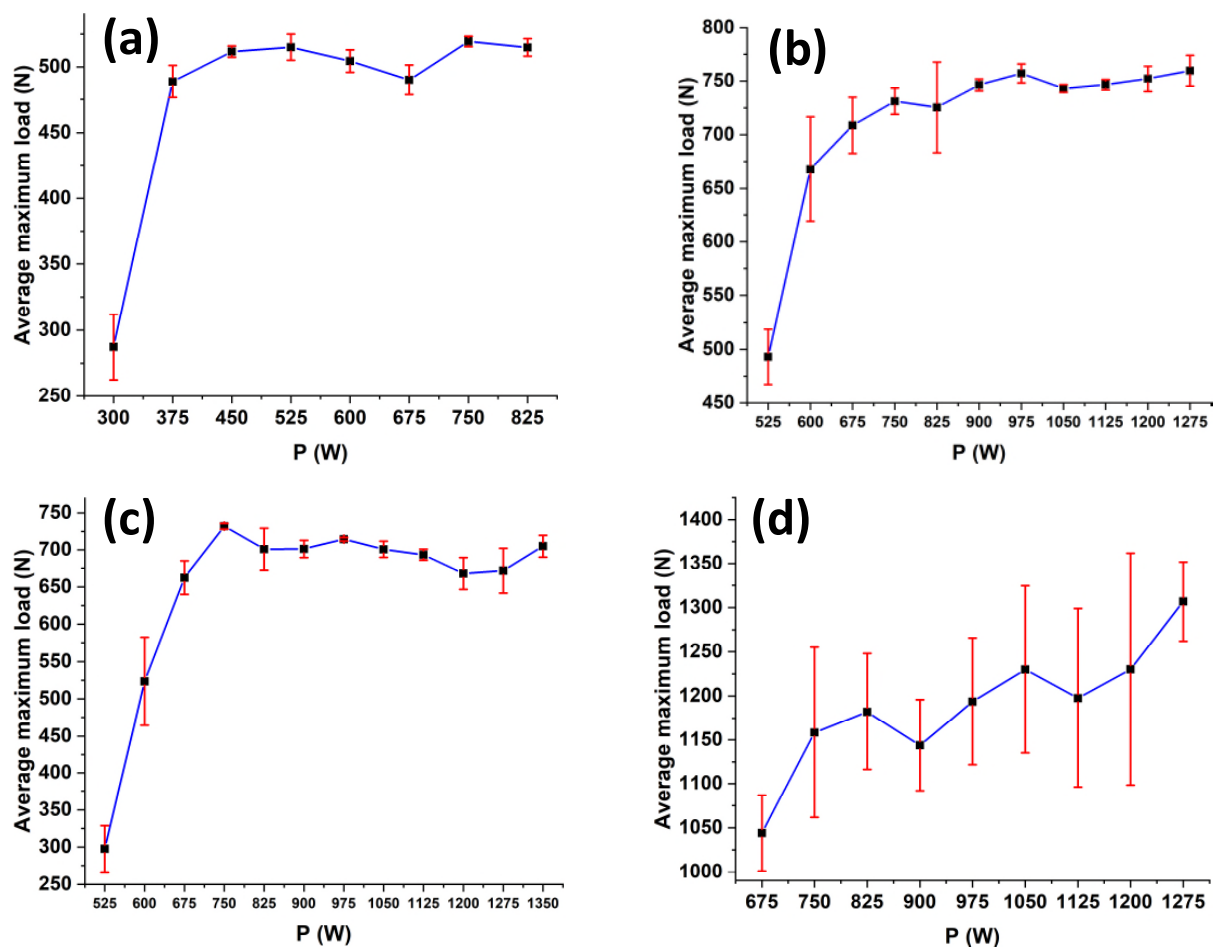

Fig. 7. Average maximum load of laser lap welded 0.3 mm (a) Al (b) Cu[Ni] (c) Cu and (d) Ni tabs to 1.5 mm Cu busbar

For example, in the Al tab to Cu busbar combination (**Fig. 7a**), the lowest joint strength of ~285 N was obtained at a laser power of 300 W and good joint strength of ~510 N was achieved at 450 W and 525 W. Also, the strength obtained from the Al tab to Cu busbar joints (285 – 510 N) was lower than for all the other tab material to Cu busbar combinations (298 – 1320 N). Al and Cu are difficult to weld together due to their different chemical and mechanical properties and the formation of IMCs, which reduce the mechanical properties like joint strength [37]. A non-consistent but overall increasing trend was obtained for the Ni tab to Cu busbar as shown in **Fig. 7(d)**. The laser power required for the Cu busbar combinations (300 – 1350 W) was more than that needed for the Al busbar (300 – 1125 W). Furthermore, the working range of laser power to produce a good weld was higher for the Cu busbar than the Al busbar combinations because the thermal conductivity of copper (i.e. $\lambda= 391.1$ W/m.K) is higher than that of aluminium (i.e. $\lambda= 229$ W/m.K). Energy savings can therefore be achieved using Al busbars rather than Cu. The laser power required for the 'good-weld' for the various tabs (i.e., Al/Cu[Ni]/Cu/Ni) to Cu busbar joints were (450 – 600 W), (900 – 1050 W), (825 - 1125 W) and (975 - 1050 W), respectively.

3.2. In-depth microstructural study

3.2.1. Various tabs to Al busbar joint

Visualising the joint formation is vital to understand the weld mechanism and the effects of the welding parameters. Therefore, the weld seam quality was determined by metallographic analysis. To investigate the welding mechanism the weld zones were categorised as under-weld, good-weld and over-weld. These categories were defined based on the load-displacement characteristics and the failure mode obtained from the lap shear tests. From visual inspection, good-welds consist of a homogeneous weld without any pores. Under-welds show very low penetration with large voids at weld interface and the over-weld showed pores, underfilling/under-cut and burn through [23, 24]. **Figures 8** to **11** show the under-weld, good-weld and over-weld for tabs to Al busbar joints observed under the optical microscope at 10x magnification. In the under-weld condition, the laser power was not sufficient to melt and fuse the tab and busbar materials properly, and thus penetration depth and weld width were small. Hence, there was a wider and larger void formed between the tab and busbar material as shown in all under-weld conditions (**Fig. 8a, 9a, 10a** and **11a**). In contrast, the over-weld conditions have an under-cut/natural notch (reduced/narrower fusion zone area, except Al tab to busbar joint) and porosity as shown in **Fig. 9c, 10c** and **11c** where local stress concentration is

significantly high enough and maybe the reason for failure at low lap shear loads. It is worth mentioning that the notch at the over-weld samples was created due to the higher laser power supply resulting in excessive heat input to melt the upper sheet. This created a large weld pool during welding that was unable to fill the weld crater during solidification [23]. However, a high penetration depth was generally obtained during over-weld. For example, a high penetration depth (530 µm) with void was obtained in the Al tab to Al busbar joint for the over-weld condition which was not desired. The welds shown in **Figures 8b**, **9b**, **10b** and **11b** are categorised under the good-weld condition due to their good weld bead profiles with moderate penetration, very low porosity/voids, and no underfilling resulting in good joint strength. These results suggest that laser power is the most significant factor in the occurrence of weld defects as well as controlling the penetration depth and weld width when welding thin tabs to thick busbars. An increase in laser power from under-weld conditions reduced the number of weld defects in terms of voids and cracks at the edge of upper and lower sheets. Therefore, to minimize the defects and optimize the penetration depth and weld width, the laser power must be restricted equal to the 'good-weld' range of process parameters corresponding to each tab and busbar joints. The voids and cracks can be seen in **Figures 8** to **11**. However, no visible cracks were observed for the under-weld and good-weld conditions except for the Al tab to Al busbar weld. Furthermore, cracks were observed on the weld bead at high laser power which was hot cracks due to stress generation during heat cycles [24]. Hot cracks were generated at higher heat input which caused distortion and therefore higher stress. Also, the thermal expansion coefficient mismatch between two materials may be one of the reasons for the generation of cracks. Hence, most cracks were visible in dissimilar material welding as shown in **Fig. 9** to **11**. Lower laser power or low heat input reduced the occurrence of cracks due to the reduction in welding stress as well and led to the formation of fine grains in the weld area due to the fast-cooling rate [23, 59]. In the work of Kumar et al. [23], the cooling rates of laser-welded samples were calculated using the following empirical formula [60]:

$$\frac{\partial T}{\partial t}\,(\mathrm{K.s^{-1}}) = \frac{2\pi\lambda\rho C_p (vd)^2}{q_0^2}(T - T_0)^3 \tag{i}$$

where, λ= thermal conductivity (W.m^{-1}.K^{-1}), ρ= material density (Kg.m^{-3}), C_p= specific heat at constant pressure (J.Kg^{-1}.K^{-1}), v= welding speed (m.s^{-1}), d = plate thickness (m), q_0= net power (W), T= reference temperature (K) and T_0= room temperature (K).

From **Eq. (i)**, the square of net power was inversely proportional to the cooling rate. Hence, the cooling rate for the lower power would be faster than the higher power. Consequently, fine grains were obtained for the lower laser power. These fine grains were less susceptible to hot cracking as the stress was more evenly distributed among numerous grain boundaries. Hence, crack formation can be prohibited by lowering laser power and localized melting.

Voids were observed in almost all the joints at the root between the tabs and busbar sheets for all the laser power values. They are normal attributed to a lack of fusion at the weld roots [24]. The lack of fusion and the existence of a little gap between the tab and busbar sheets failed to produce a continuous weld at the weld root, thus leading to the formation of a void. Larger cracks were observed in the specimens welded with high laser power. The cracks originated from the voids, rapidly propagated towards the tab material due to the weld solidification direction which consequently reduces the joint strength of specimens. The Ni tabs required the highest power (900 W) for the good-weld, followed by Cu (825 W) and Cu[Ni] (600 W), whilst, the lowest power was required for the Al tab (525 W) due to its low melting point (see **Table 3**).
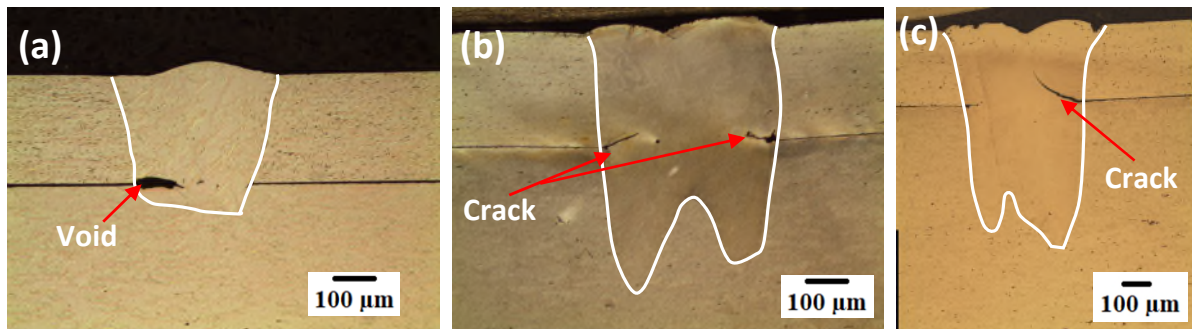

Fig. 8. Macro view of the laser welded Al tab to Al busbar at (a) under-weld, P= 300 W (b) good-weld, P= 525 W and (c) over-weld, P= 675 W
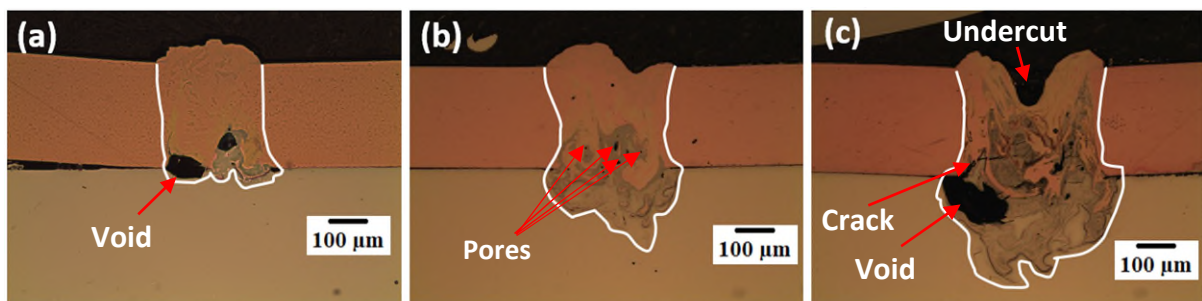

Fig. 9. Macro view of the laser welded Cu[Ni] tab to Al busbar at (a) under-weld, P= 525 W (b) good-weld, P= 600 W and (c) over-weld, P= 900 W
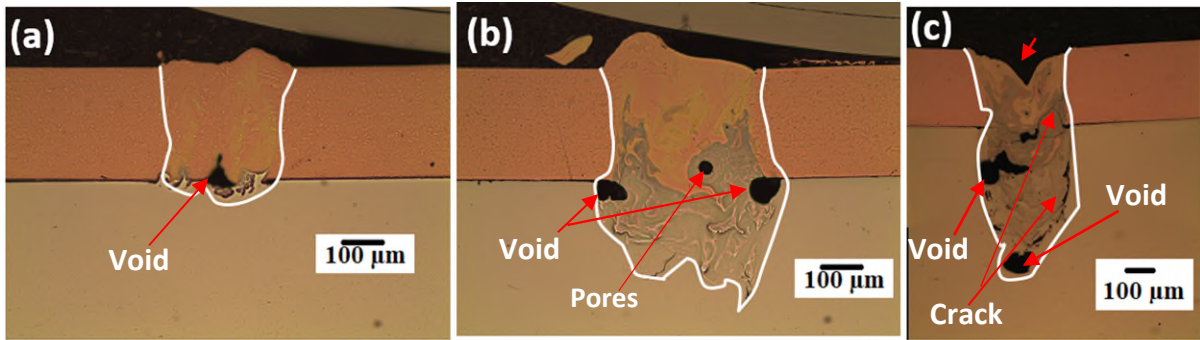
Fig. 10. Macro view of the laser welded Cu tab to Al busbar at (a) under-weld, P= 525 W (b) good-weld, P= 825 W and (c) over-weld, P= 1125 W
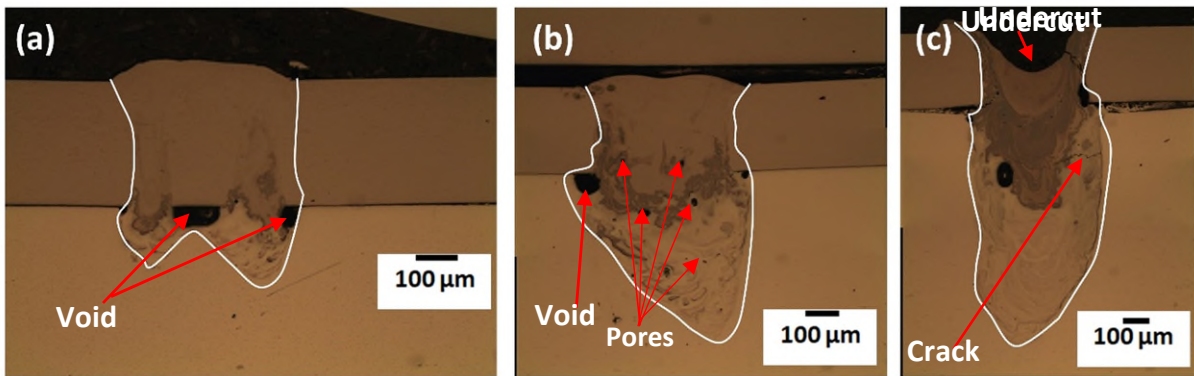

Fig. 11. Macro view of the laser welded Ni tab to Al busbar at (a) under-weld, P= 450 W (b) good-weld, P= 900 W and (c) over-weld, P= 1125 W

3.2.2. Various tabs to Cu busbar joint

In this section, the weld cross-sections of the various material tabs to Cu busbar joints were categorised for under-weld, good-weld and over-weld conditions following examination under the optical microscope at low magnification (i.e., 10x magnification). As seen from **Figures 12** to **15**, the seam geometry in the tab sheets was almost identical to those with the Al busbar, but the penetration depth into the bottom sheet was significantly smaller due to their high thermal conductivity and melting temperature of Cu. For the tab to Cu busbar joints, high penetration depths were not required to achieve a good quality weld. Also, no cracks were visible due to the low-stress generation during heat cycles or after solidification owing to lower thermal expansion coefficients of Cu (16×10^{-6} °C^{-1}) than Al (24×10^{-6} °C^{-1}). The laser power required for the good quality weld for the Cu[Ni], Cu and Ni tabs to busbar joints were equal i.e. 975 W. In contrast, the power required for the Al tab was only 525 W due to its low melting point. Pores visible in some of the welded joints (**Figs. 9, 10, 11** and **13**) occurred due to the difference in the physical, mechanical properties and solubility problem of the tab and busbar materials and will be discussed in detail in section 3.2.3.

Fig. 12. Macro view of the laser-welded Al tab to Cu busbar at (a) under-weld, P= 300 (b) good-weld, P= 525 W and (c) over-weld, P= 825 W

Fig. 13. Macro view of the laser-welded Cu[Ni] tab to Cu busbar at (a) under-weld, P= 525 W (b) good-weld, P= 975 W and (c) over-weld, P= 1275 W

Fig. 14. Macro view of the laser-welded Cu tab to Cu busbar at (a) under-weld, P= 525 W (b) good weld, P= 975 W and (c) over-weld, P= 1275 W

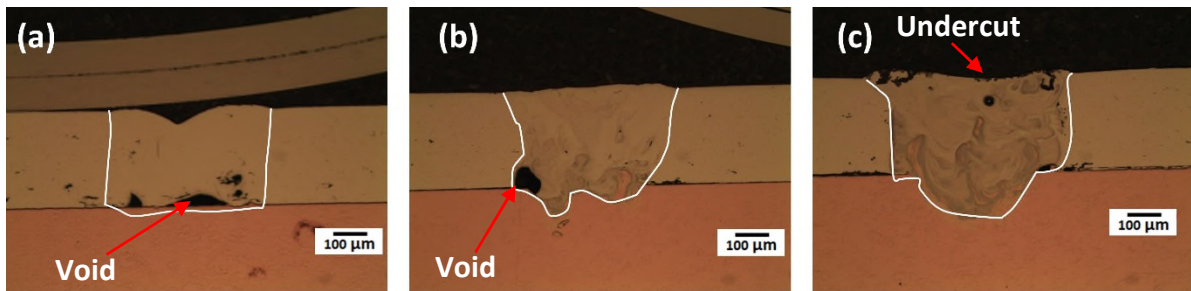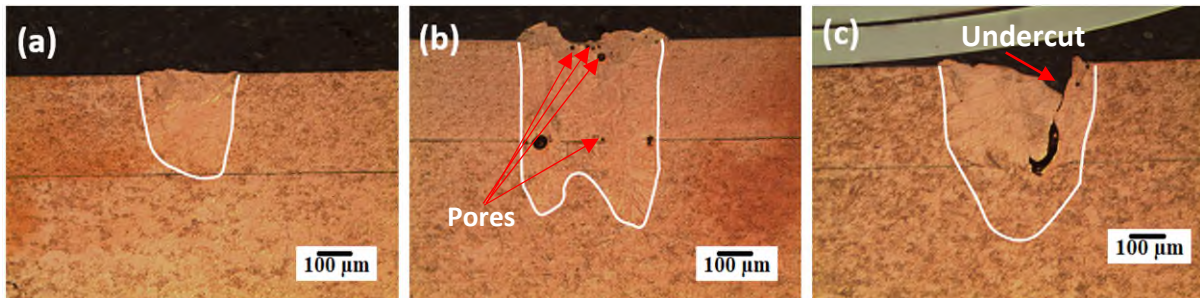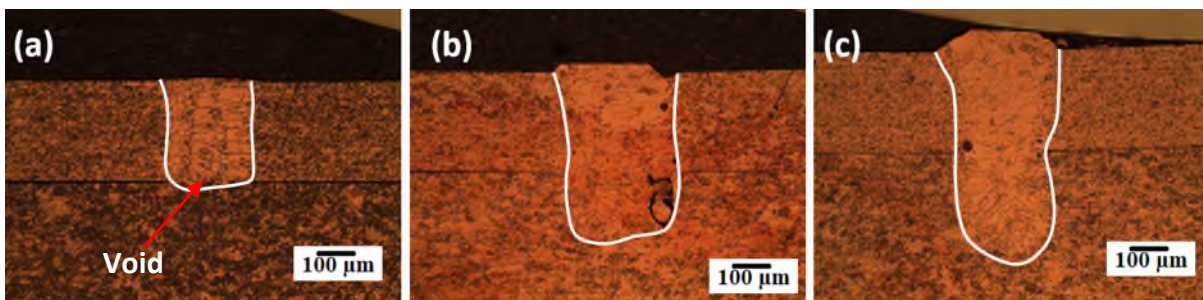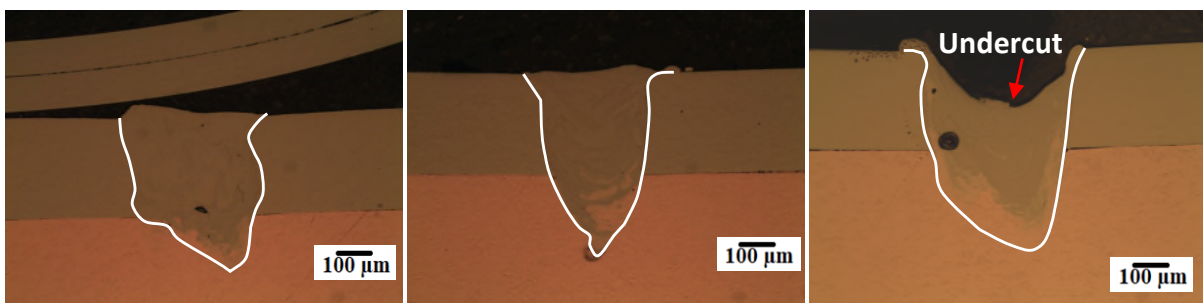**Fig. 15.** Macro view of the laser-welded Ni tab to Cu busbar at (a) under-weld, P= 675 W (b) good-weld, P= 975 W and (c) over-weld, P= 1275 W

3.2.3. IMCs study

In this section, the phases formed in the laser-welded sample were studied. Although formed in the same reaction system, various microstructures can be obtained in different regions of the laser-welded fusion zone due to the high thermal gradient of the laser welding process [40]. Four tab-to-busbar combinations were selected for this intermetallic analysis to study the dissimilar material joints: Cu tab to Al busbar, Al tab to Cu busbar, Ni tab to Al and Cu busbar, when welded using parameters for a good weld condition. The weld micrographs are shown in **Figs. 16 – 19** respectively. The possibility of IMC formation was maximum for these samples. IMCs formation, in the case of dissimilar metal welding, was identified using EDX, reported by several researchers [39-42, 47-48, 58]. Hence, the energy dispersive X-ray (EDX) analyser of the scanning electron microscope (SEM) was used to determine the composition of the compounds formed along the lines L1, L2 and L3, and at the points A, B, C, D, E, F, G, H shown in the figures. SEM images of the Cu tab to Al busbar laser weld are shown in **Figs. 16(a)** and **(b)**. Micro-cracks are visible in the fusion zone (FZ) and propagate into (Al) solid solution as shown in **Fig. 16(b**) and can be attributed to the large difference in the thermal expansion coefficients of aluminium (24×10^{-6} $°C^{-1}$) and copper (16×10^{-6} $°C^{-1}$). The characteristic of fast heating and cooling of laser welding easily generates stresses which cause solidification cracks [51]. No micro-cracks were visible in the cross-section of Al tab to Cu busbar weld (**Fig. 17a**). This may be due to a decrease in stress caused by increasing the Cu thickness from 0.3 mm (i.e., tab) to 1.5 mm (i.e., busbar), which acted as a more effective heatsink. Also, the heat input required to produce a good-weld for the Al tab to Cu busbar joint is lower (525 W) than the Cu tab to Al busbar joint (825 W). In the latter case, the high energy input creates a steep thermal gradient at the weld zone and high thermal stress is generated. The EDX line results of the Cu tab to Al busbar joint are shown in **Fig. 16(c)** and the chemical composition analysis of elements at various points (i.e. A, B, C, …..G, H) are listed in **Fig. 16(d)**. Similarly, the SEM morphologies and EDX results of the Al tab to Cu busbar joint are shown in **Fig. 17**. **Fig. 17(a)**, shows that the diffusion/mixing of Al tab metal into Cu base is very low in comparison with **Fig. 16(a)** for the Cu tab to Al base joint. From **Fig. 16(b)**, it is obvious that the interface zone along the direction from pure copper to Al weld metal zone is composed of the (Cu) solid solution in the positions of points A and C, CuAl in the positions of points B, D and E, $CuAl_3$ in the positions of point F and (Al) solid solution in the positions of points G and H [39, 40]. Whereas for the Al tab to Cu, (Al) solid solution occurs positions of points A, B and C, $CuAl_2$ in the positions of point D and (Cu) solid solution in the positions

of point F [40] as shown in **Fig. 17(b)**. During the laser welding of dissimilar metals, two kinds of atoms combine to form a range of IMC dependant on the relative concentrations throughout the fusion zone. Zuo et al. [44] proved that the $CuAl_2$ IMC of the interface zone can weaken the shear strength joint. Several studies have proved that the formation and growth of intermetallic compounds of Cu/Al or Al/Cu in the interface zone can influence the comprehensive (e.g., Joint strength, resistance etc.) properties of joints [44 – 46]. These phases were determined by EDX analyses, as tabulated in **Fig. 16(d)** and **Fig. 17(d)**. The zone where (Cu) and (Al) solid solution was obtained because the Cu and Al elements can unlimitedly intermix each other [40, 43]. Furthermore, the white arrows in **Fig. 16(b**) and **Fig. 17(b)** demonstrated the EDX line scanning direction. **Fig. 16(c)** and **Fig. 17(c)** shows the EDX line scan (i.e., L1, L2 and L3) results of Cu tab to Al busbar and Al tab to Cu busbar joints, which shows the changes in concentration of the Al and Cu and vice-versa, respectively, and the weld interface layers were pointed out in figures. According to the EDX line result, it can also be concluded that the contents of tab and busbar elements were transferred (mixing) smoothly in weld metal (fusion zone). It is evident from **Fig. 16(c)** that the Cu and Al concentrations present a gradient distribution along the line L2. Whereas, in **Fig. 17(c)** the Al and Cu concentration present a gradient distribution along all the lines (i.e., L1, L2 and L3). In addition, it is clear from **Fig. 16(c)** and **Fig. 17(c)**, that a large fluctuation exists in the Al to Cu EDX line scan distribution curves than Cu to Al distribution curve. A little amount of curve overlap means that only a small amount of intermetallic compounds were generated in the welded joints [50]. Hence, the formation of IMCs at the Al tab to Cu busbar joints should be more than the Cu tab to Al busbar joints. This may be the probable cause of obtaining slightly lower strength from the Al tab to Cu busbar joints (about 520 N) than the Cu tab to Al busbar joints (about 560 N). Also, the $CuAl_2$ IMCs were formed at the weld interface of the Al tab to Cu busbar joints, which can weaken the strength of the joint [51]. It is also evident from the map scanning results of elements distribution obtained at the cross-sections of Cu tab to Al busbar and Al tab to Cu busbar weld joints as demonstrated in **Fig. 16(e)** and **Fig. 17(e),** that the diffusion rate and diffusion amount of tab base metal to the busbar base metal was very low in case of Al tab to Cu busbar joint which causes lack of penetration. Consequently, low joint strength was obtained for Al to Cu busbar joint. It is also obvious from **Fig. 16(e)** and **Fig. 17(e)**, that both Al and Cu elements were unevenly distributed in weld pools.

Fig. 18 and **Fig. 19** shows the SEM morphologies and EDX results of Ni tab to Al and Cu busbar joints respectively. From **Fig. 18(b)**, the Ni parent metal melted sharply and then mixed

into the weld and IMCs formed in the weld during cooling, and thus the weld might be fractured spontaneously under the action of welding residual stress [42]. According to Al-Ni phase diagram reported by Massalski [49], the microstructures are formed by two following peritectic reactions in sequence: $AlNi + L \rightarrow Al_3Ni_2$ and $Al_3Ni_2 + L \rightarrow Al_3Ni$. In the welding pool, there was a mass of the Ni because liquid Ni mixed into liquid metal by diffusion and convection. The Al base metal in the weld strongly diffused to liquid Ni layer due to the stirring/wobble impact of the weld pool. The Ni content raised rapidly to a high level. Therefore, two peritectic reactions appeared in the melted Ni layer during cooling, and the peritectic reaction $L + Al_3Ni_2 \rightarrow Al_3Ni$ occurred in the weld pool (**Fig. 18d**). Finally, with decreasing temperature to the eutectic temperature, the liquid metal solidified, and the weld consisted with Al_3Ni in the positions of points C and E and (Al) solid solution in the positions of points A, D, F, G, H and (Ni) solid solution in the positions of point B. Also, the Al_3Ni was a major reason for forming the pores (i.e., clearly point out in **Fig. 11b**). First, the Al_3Ni provided a mass of solid/liquid interfaces for heterogeneous nucleation of the pores. Second, the viscosity of the pool increased because the solid Al_3Ni precipitated, which obstructed the floating of the pores [42]. In the research of Chen et al. [42], they also found that the joint strength of Ni/Al joint was inversely proportional to the IMCs density. It is evident from **Fig. 18(c)** that a large fluctuation exists in the Ni to Al, EDX line scan distribution curves along all the line scan paths i.e., L1, L2 and L3. Then a large amount of IMCs would have been formed in the case Ni and Al joints, which might have effectively reduced the tensile strength of the welded joint [42]. In addition, it can also be concluded from the map scanning results of weld cross-sections of Ni tab to Al busbar, as shown in **Fig. 18(e),** that the diffusion rate and diffusion amount of base metals was very high.

The cross-sectional morphology and their enlarged image of Ni tab to Cu busbar welded joints are shown in **Fig. 19(a)** and **Fig. 19(b)** respectively. **Fig. 19(c)** and **(d)** show the line scan and point scanning results of **Fig. 19(b)**, and **Fig. 19(e)** shows the elemental distribution of Ni and Cu of **Fig. 19(a)**. It is evident from **Fig. 19(d)** that Ni and Cu concentrations present a gradient distribution along all the line scan paths (i.e., L1, L2 and L3). As discussed in section 3.1, the maximum joint strength was obtained for the Ni tab to Cu busbar joints about 1320 N followed by Ni tab to Al busbar joints about 930 N. Also, it was observed from section 3.2, that the weld morphology obtained from the Ni tab to Cu busbar joint was quite good (i.e., the cross-section of Ni tab to Cu welded samples showed no visible defect) in comparison with other combinations of tab and busbar joints. Hume-Rothery [53] generalized several rules on solid

solutions in alloy systems, including (i) the difference in the atomic size between the solute and solvent atoms must be less than 15%, (ii) the crystal structures of the solute and solvent must match, (iii) there are the same valence states between the solvent and solute, and (iv) the solute and solvent should have similar electronegativity. For generations, Hume-Rothery rules have been used in the traditional alloying design. Generally, a solid solution is often observed when the two elements (generally metals) involved are from the same family in the periodic table (i.e., the same column). Conversely, a chemical compound forms when the Hume-Rothery rules are not satisfied. The binary Cu–Ni phase diagram [54] is an example of Hume-Rothery rules which satisfied all 4 rules, the metals like Cu and Ni show complete solid solubility from 100% copper to 100% nickel, i.e., they are soluble in each other in the solid-state in any proportion to give a series of solid solutions (having different proportions of metals), but with the same single FCC crystal structure [52]. The more the difference in the atomic size of the solute atom and the solvent atom, the smaller is the solid solubility. For complete solid solubility, the size factor must be less than 8%. The atomic diameters differ by more than 15%, the size factor is unfavourable, and the solid solubility is low. The metals like nickel and copper the difference in atomic size is about 2.7% and has the same crystal structure, which is FCC, and show complete solid solubility [52]. In the research of Yan et al. [51], an in-depth IMCs study was conducted for the dissimilar joint consists of 6061 aluminium and 110 coppers with a Ni interlayer, and they were not found any phase between Ni-Cu. Also, Shamsolhodaei et al. [55] were studied the laser welding NiTi-copper, and they weren't found any IMCs phases related to Ni-Cu. Moreover, our results of EDX showed (**Fig. 19d**) that there was no solute segregation in the Ni tab to Cu busbar weld joints, indicating that a uniform composition of a weld under the convection effect in the welding process was achieved, which was significant to improve the mechanical properties of the joint over other combination of tab and busbar joints conducted in this study.
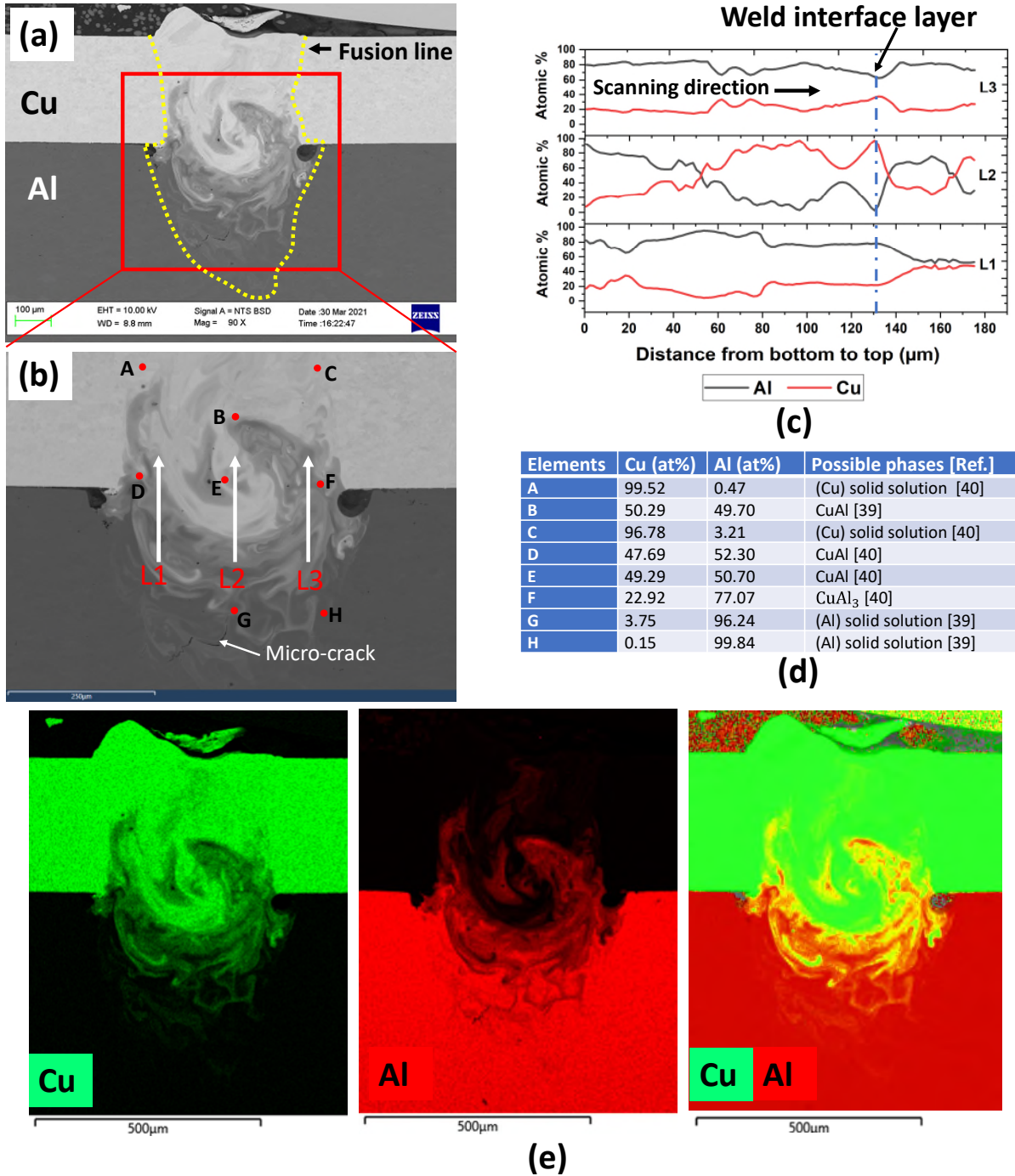
Fig. 16. (a) SEM image of the laser welded Cu tab to Al busbar at P= 825 W (b) enlarged view of the weld region (c) EDX line scanning results of figure 16b (d) EDX scan at points A, B, C, D, E, F, G, H of figure 16b to specify the phase composition and (e) Cu and Al elements distribution of figure 16a

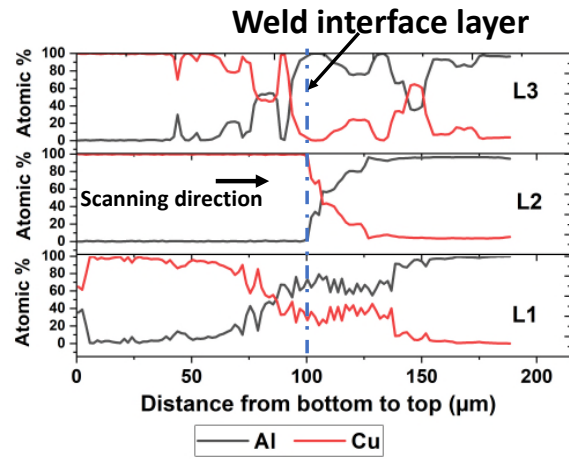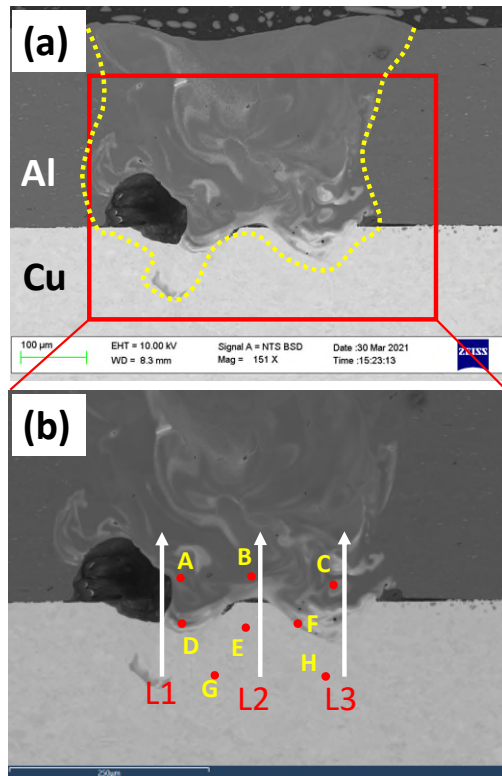| Elements	Cu (at%)	Al (at%)	Possible phases [Ref.]
A	99.52	0.47	(Cu) solid solution [40]
B	50.29	49.70	CuAl [39]
C	96.78	3.21	(Cu) solid solution [40]
D	47.69	52.30	CuAl [40]
E	49.29	50.70	CuAl [40]
F	22.92	77.07	CuAl$_3$ [40]
G	3.75	96.24	(Al) solid solution [39]
H	0.15	99.84	(Al) solid solution [39]

Fig. 17. (a) SEM image of the laser welded Al tab to Cu busbar at P= 525 W (b) enlarged view of the weld region (c) EDX line scanning results of figure 17b (d) EDX scan at points A, B, C, D, E, F, G, H of figure 17b to specify the phase composition and (e) Al and Cu elements distribution of figure 17a

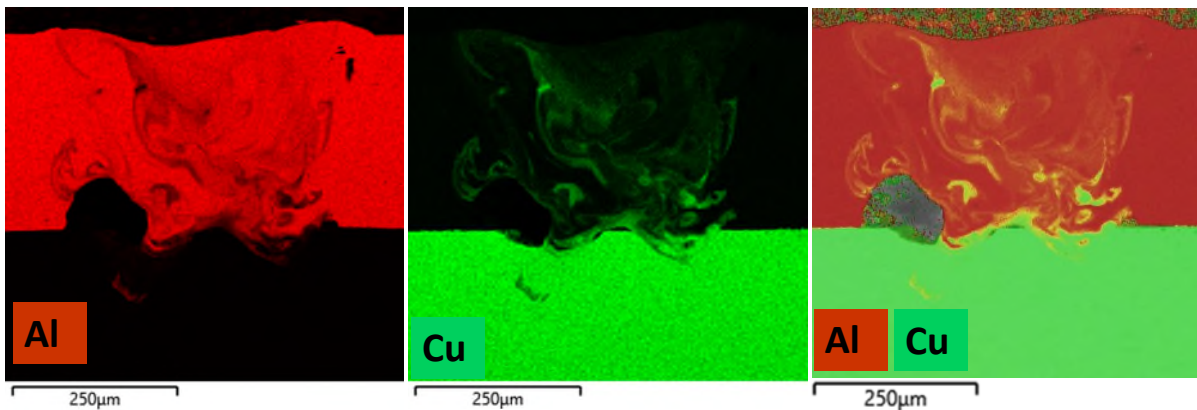| Elements	Al (at%)	Ni (at%)	Possible phases [Ref.]
A	96.26	3.73	(Al) solid solution
B	17.95	82.04	(Ni) solid solution [42]
C	85.81	14.18	Al_3Ni [41]
D	98.04	1.95	(Al) solid solution
E	89.65	10.34	Al_3Ni [41]
F	100	0	(Al) solid solution
G	99.63	0.36	(Al) solid solution
H	100	0	(Al) solid solution

Fig. 18. (a) SEM image of the laser welded Ni tab to Al busbar at P= 900 W (b) enlarged view of the weld region (c) EDX line scanning results of figure 18b (d) EDX scan at points A, B, C, D, E, F, G, H of figure 18b to specify the phase composition and (e) Ni and Al elements distribution of figure 18b

(a)

Ni

Cu

100 µm — EHT = 10.00 kV — Signal A = NTS BSD — Date :30 Mar 2021
WD = 8.2 mm — Mag = 120 X — Time :13:33:26 — ZEISS

(b)

A B C D E

F G H

L1 L2 L3

250µm

Weld interface layer

Scanning direction →

L3

L2

L1

Atomic %

Distance from bottom to top (µm)

— Ni — Cu

(c)

Elements	Cu (at%)	Ni (at%)	Possible phases [Ref.]
A	41.69	58.30	(Cu, Ni) solid solution [47]
B	22.64	77.35	(Cu, Ni) solid solution [47]
C	50.02	49.97	(Cu, Ni) solid solution [47]
D	9.75	90.24	(Cu, Ni) solid solution [48]
E	85.96	14.03	(Cu, Ni) solid solution [48]
F	98.62	1.377	(Cu, Ni) solid solution [47]
G	79.56	20.43	(Cu, Ni) solid solution [47]
H	100	0	Cu solid

(d)

Ni — 250µm

Cu — 250µm

Ni Cu — 250µm

(e)

Fig. 19. (a) SEM image of the laser welded Ni tab to Cu busbar at P= 975 W (b) enlarged view of the weld region (c) EDX line scanning results of figure 19b (d) EDX scan at points A, B, C, D, E, F, G, H of figure 19b to specify the phase composition and (e) Ni and Cu elements distribution of figure 19a
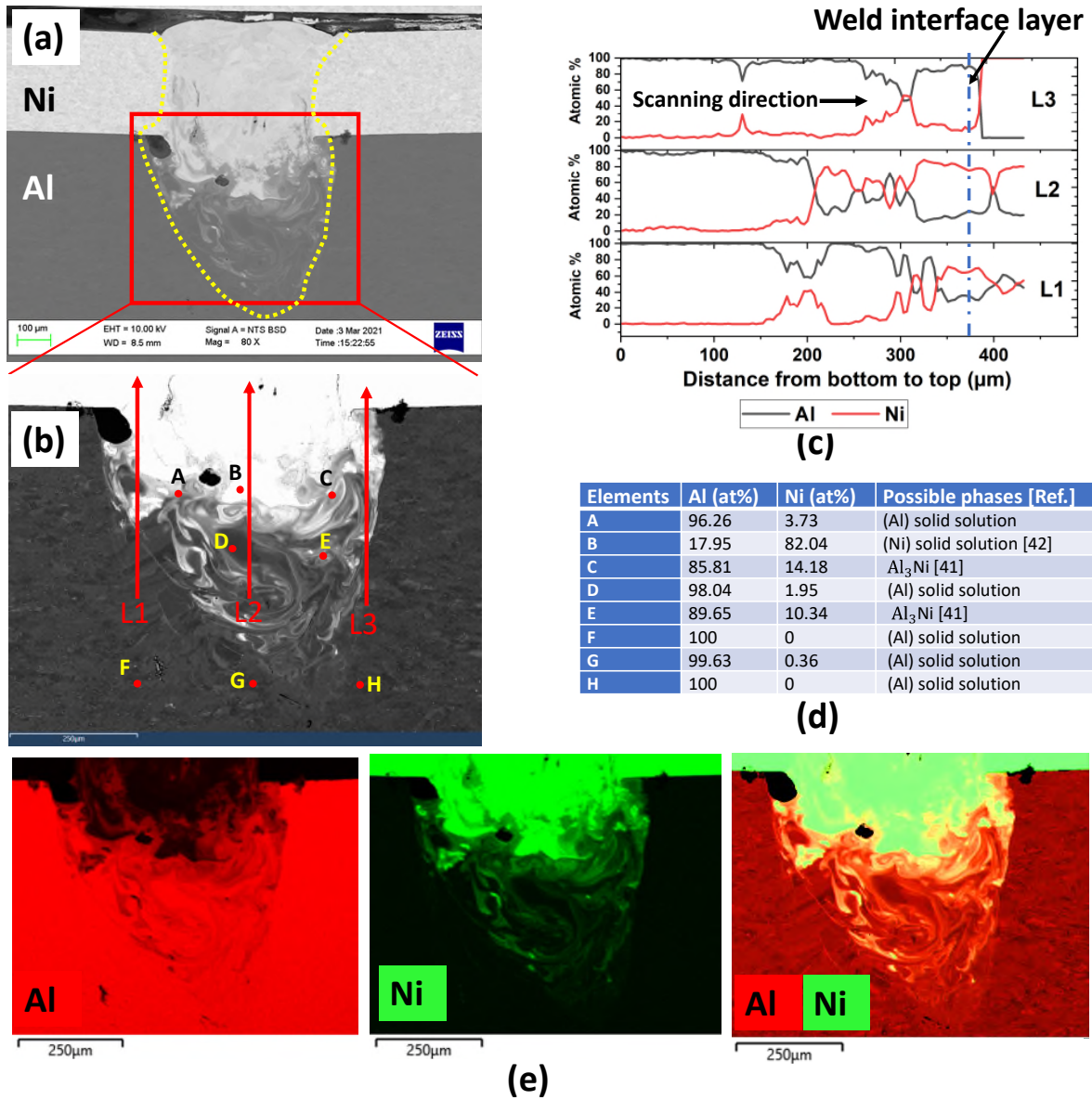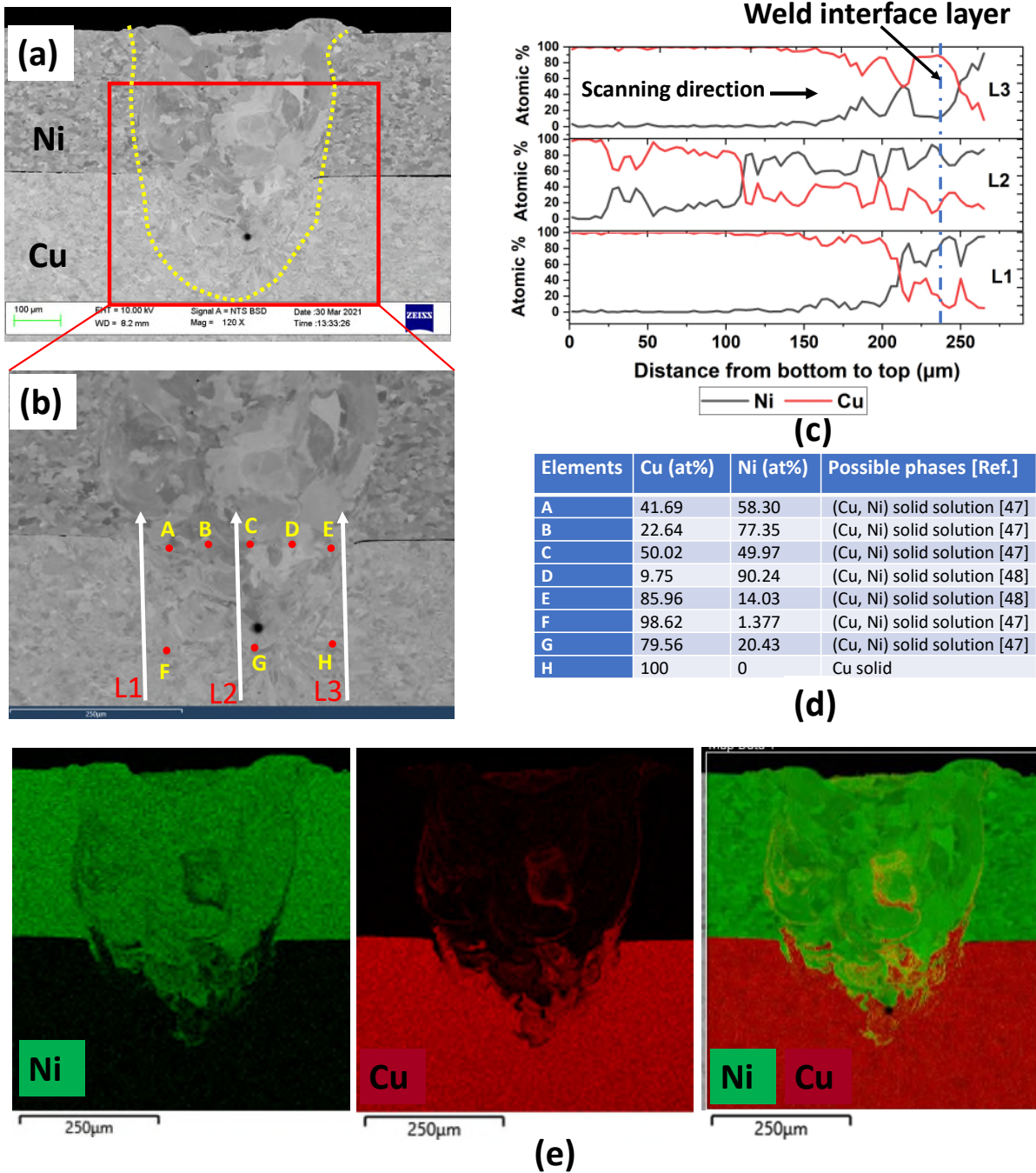
3.2.4. Electrical contact resistance profile

The electrical contact resistance was determined from the measured induced voltage across the laser-welded joint using the voltage measuring pin as per the test set-up described in section 2. **Fig. 20** and **21** show the measured electrical contact resistance for the various tabs (Al/Cu/Cu[Ni]/Ni) to Al and Cu busbars respectively. The resistance of Ni tab at 200 A current was not presented due to the overheating (by about 400 °C) of the specimen after 30 s of applied current as shown in **Fig. 22**. The change in resistance was measured for 180 s at different amplitudes of current (i.e. 100 A, 150 A and 200 A) passed through the joints. Sufficient voltage measurements (i.e. total= 180, captured at 1s interval) could be taken within the test time to eliminate the effects of drift during the measurement cycle. A high supply current was necessary, requiring maximum energy storage capability, amperage and voltage, to deliver the necessary power and driving range, to ensure a high measurement accuracy because the deviations of the supply current from the power source decreases with increasing currents, while the precision of the multimeter increases. The specimens produced under good-weld parametric conditions, as defined in sections 3.2.1 and 3.2.2, were chosen for the resistance and temperature inspection. From **Fig. 20** and **21**, it can be noted that after an initial fast rise the resistance only slowly increasing within the period of applied current. When the current is increased the rate of rising in the resistance also increases. When the current was passed through the welded specimens, resistive heat loss generated heat increased the resistance of the joint and worked as a positive feedback loop [26]. The curves from the Cu and Cu[Ni] tabs to either Al or Cu busbar joints were almost congruent. As shown in **Table 3** the Cu and Cu[Ni] tabs have almost similar mechanical and electrical properties**.** The lowest contact resistance was measured for the Cu tab among the four materials investigated. For the Cu tab to Al busbar joints, the value of resistance at the beginning was around 0.051 mΩ irrespective of the applied current. At the end of 180 s of the current application, the resistance increased to 0.053 mΩ for 100 A, 0.056 mΩ for 150 A and 0.066 for 200 A, about 4%, 10% and 30% increase in resistance respectively. Similarly, for Cu to Cu busbar, the value of resistance at the beginning of the measurement was around 0.042 mΩ, and at the end of 180 s, the resistance increased close to 0.044 mΩ for 100 A current, 0.048 mΩ for 150 A current and 0.050 mΩ for 200 A (i.e. increased by about 5%, 14% and 19%) respectively. The highest contact resistance values were obtained for the Ni tab followed by Al tab for both the Al and Cu busbar material combinations. These are due to the highest electrical resistivity values of Ni (7×10^{-8} Ω.m) followed by Al (2.8×10^{-8} Ω.m), Cu[Ni] ($\rho = 1.9 \times 10^{-8}$ Ω.m) and Cu ($\rho = 1.7 \times 10^{-8}$ Ω.m). Electrical resistivity (ρ)

is an intrinsic property of a material and is directly proportional to the total resistance (Ω). For Ni tab to Al busbar, the value of resistance at the beginning of the test was around 0.169 mΩ, at the end of 180 s current flow, the resistance reached at 0.238 mΩ for 100 A and 0.29 A for 150 A, which were about 41% and 72% increase respectively. Similarly, for Ni tab to Cu busbar, the value of resistance at the beginning of the test was around 0.168 mΩ, at the end of 180 s current flow, the resistance increased close to 0.187 mΩ for 100 A and 0.243 A for 150 A current, which were increased by about 12% and 45% respectively.
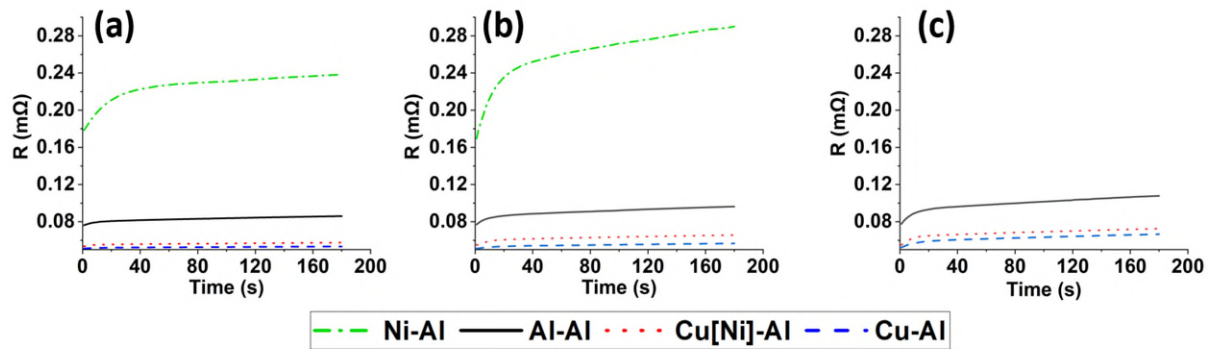

Fig. 20. Electrical resistance measurement of the various tab to Al busbar welded sample at (a) 100A (b) 150A and (c) 200A
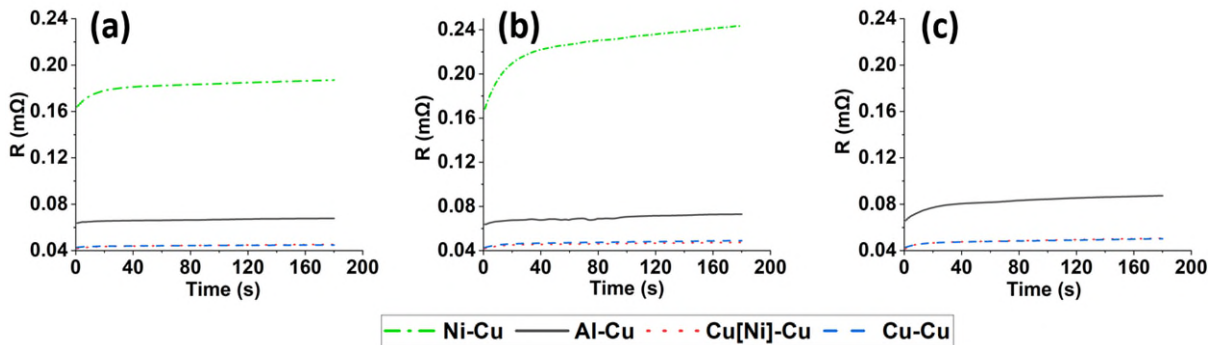

Fig. 21. Electrical resistance measurement of the various tab to Cu busbar welded sample at (a) 100A (b) 150A and (c) 200A

The contact resistance and relative changes obtained from the tabs to Cu busbar joints were smaller in comparison to the tabs to Al busbar joints because Cu has lower electrical resistivity (1.7×10^{-8} Ω.m) than Al (2.8×10^{-8} Ω.m). Additionally, the copper has faster heat dissipation (i.e. $\lambda = 391.1$ W/m.K) properties than aluminium (i.e. $\lambda = 229$ W/m.K). As a result, a low rise in resistance was observed for the Cu busbar data over the Al busbar. The lowest resistance was obtained for the Cu tab to Cu busbar joints among all combinations of tab and busbar joints as shown in **Fig. 20** and **21**. Cu is traditionally used as busbar material; however, Al busbars are gaining popularity due to cost and weight savings. From **Fig. 20**, the resistance obtained for

the Cu tab to Al busbar joint is about (16 – 20%) more than the resistance obtained for the Cu tab to Cu busbar joint as shown in **Fig. 21**. But the selection of Al busbar can reduce the cost and weight of the busbar usage by about 75% within a battery module as shown in **Table 3**.
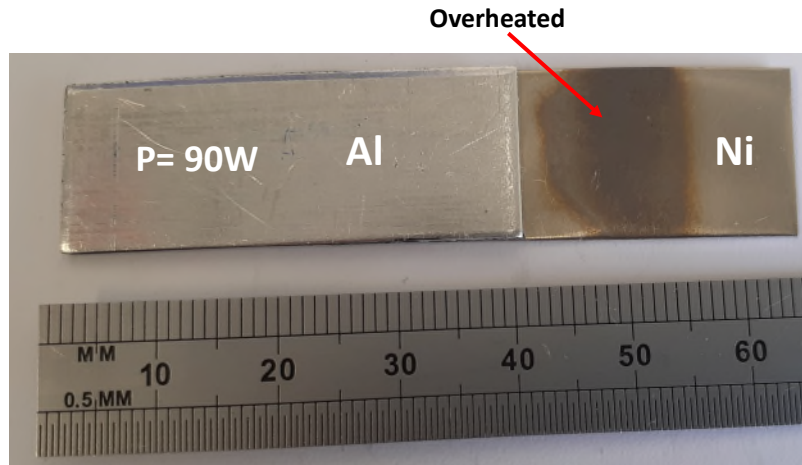

Fig. 22. Condition of laser welded Ni tab to Al busbar (bottom view) after passing 200 A current for 30 s

3.2.5. Joint temperature profile

As electrical contact resistance is temperature dependent [25], it is necessary to describe the electrical resistances variation with respect to temperature. Due to the effect of Joule heating, the current-carrying laser welded samples warm up during the cycle of the current flow (i.e. representative of the charge-discharge cycle of the vehicle) [22]. The subsequent temperature rise was captured when currents of 100 A, 150 A and 200 A passed through the joints for 180 s each. **Fig. 23** and **24** shows the results for the various tab to Al and Cu busbar joints respectively. All results were measured from a room temperature of 23.6°C. The rise in temperature for Ni tab at 200 A current was not presented due to the overheating (by about 400°C) of the specimen after the 30 s of applied current. The maximum temperatures measured were for the Ni tab to Al busbar joints, 89.9°C for 100 A and 157.8°C for 150 A, whereas minimum values were for the Cu tab to Cu busbar joints, 34°C for 100 A, 46.5°C for 150 A and 68.4°C for 200 A. This corresponds to resistance measurements reported in Section 3.2.4. The temperature and resistance are consistent with the effect of Joule heating ($I^2 R_{weld}$). **Figs. 25 - 27** shows the IR thermal image of the various tabs to Al and Cu busbar joint area at 100 A, 150 A and 200 A respectively, captured at t= 180 s and **Table 5** shows the rise in temperature for the various joints after 180 s. The highest temperature rise was obtained for the Ni tab followed by Al, Cu[Ni] and Cu tabs for both the Al and Cu busbar material combinations.

These are due to the highest thermal conductivity values of Cu (λ= 391.1 W/m.K) followed by Cu[Ni] (λ= 354.23 W/m.K), Al (λ= 229 W/m.K) and Ni (λ= 70.2 W/m.K). Thermal conductivity (λ) is an intrinsic property of a material and is inversely proportional to the rise in temperature of the welded sample (**Eq. i**). It is evident from **Eq. (i)**, that the cooling rate is directly proportional to the thermal conductivity of the base metal [61]. Hence, the maximum temperature was obtained for the Ni tab due to the slow cooling rate. Whereas, the minimum for the Cu tab is due to the fast cooling rate.
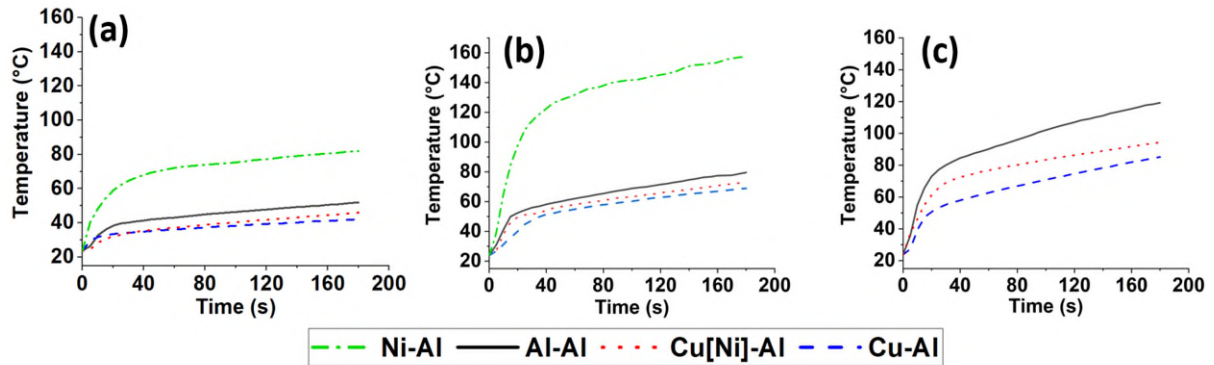

Fig. 23. Temperature measurement of the various tab to Al busbar welded sample at (a) 100 A (b) 150 A and (c) 200 A
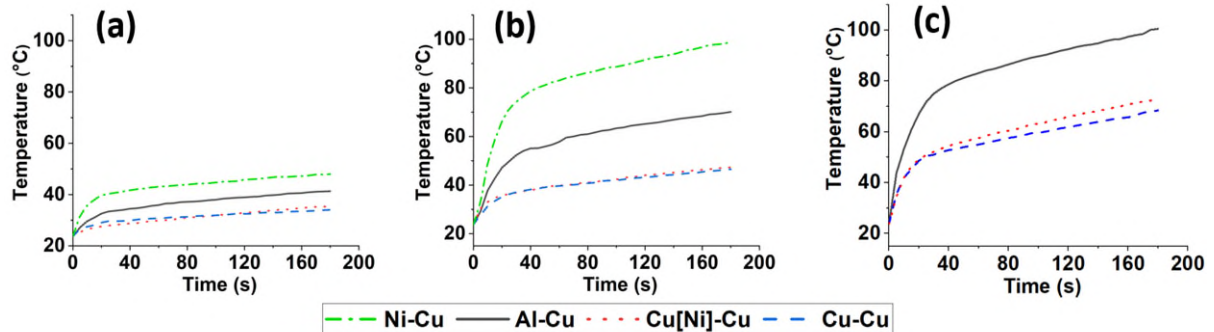

Fig. 24. Temperature measurement of the various tab to Cu busbar welded sample at (a) 100 A (b) 150 A and (c) 200 A

In this experiment, the welded coupons are bare and open to the environment. In service, however, the welded joints would be enclosed within the confines of the battery box and expected to reach higher temperatures. Although commercial battery packs have an active or passive thermal management system (TMS), these are mainly designed to focus on surface cooling of the cells, rather than the busbar. Therefore, temperature hotspots could still exist within a battery pack having a TMS [38]. The rise in joint temperature is recognized as one of the critical stress factors which could affect battery performance. Exposing the battery cells to high temperatures can accelerate ageing and promote solid electrolyte interface growth leading

to premature failure [26, 33]. The results presented here indicate the significance of selecting the correct tab and busbar material combinations to minimise the detrimental effects of high joint temperature as it is commonly held that the Li-ion battery can safely operate at 45ºC [26].

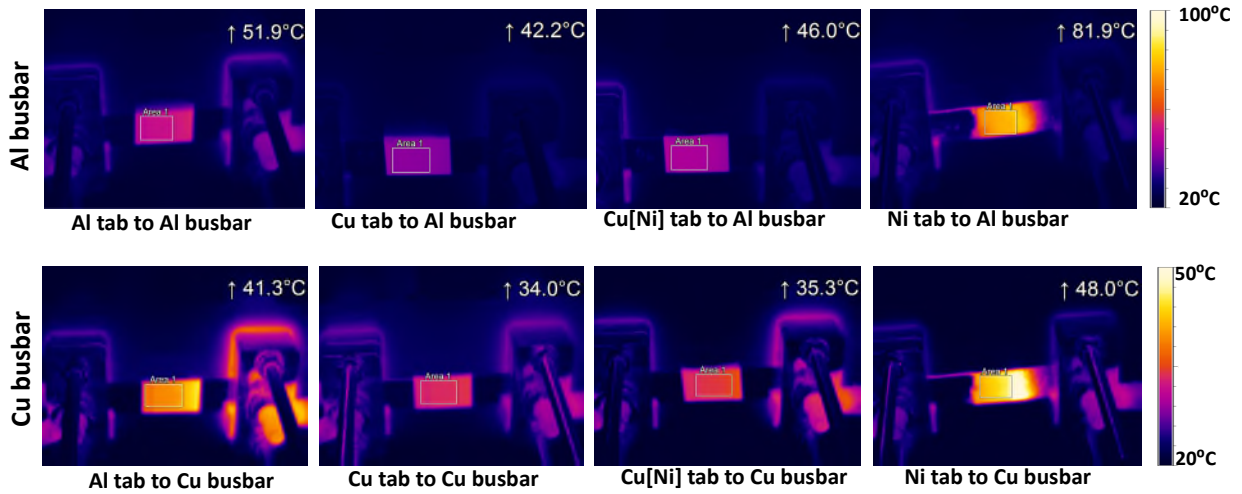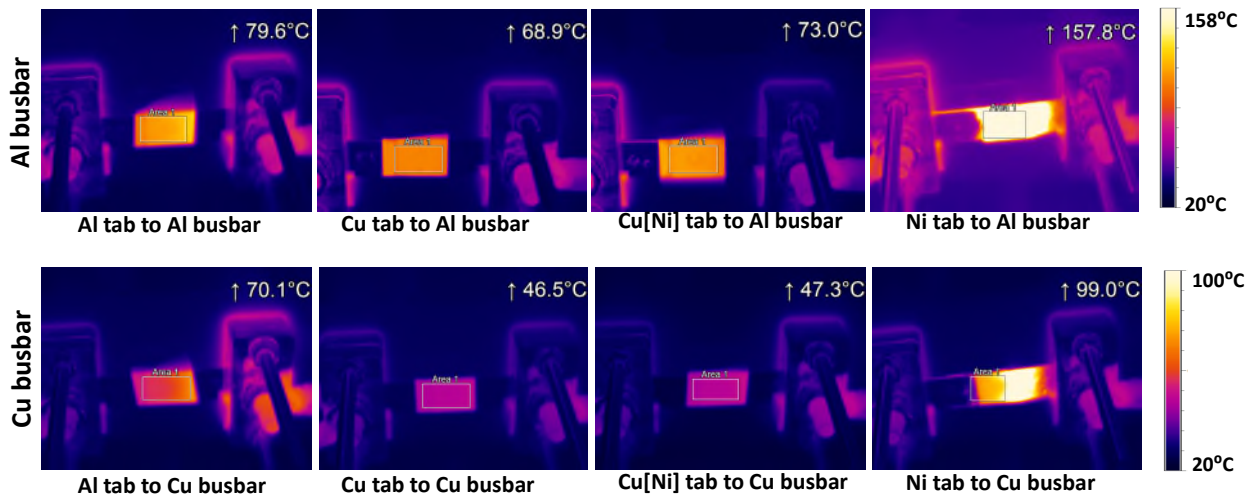**Fig. 25.** IR thermal images as a result of current flow from various tabs to Al and Cu busbar joint at t= 180s at 100 A

Fig. 26. IR thermal images as a result of current flow from various tabs to Al and Cu busbar joint at t= 180s at 150 A
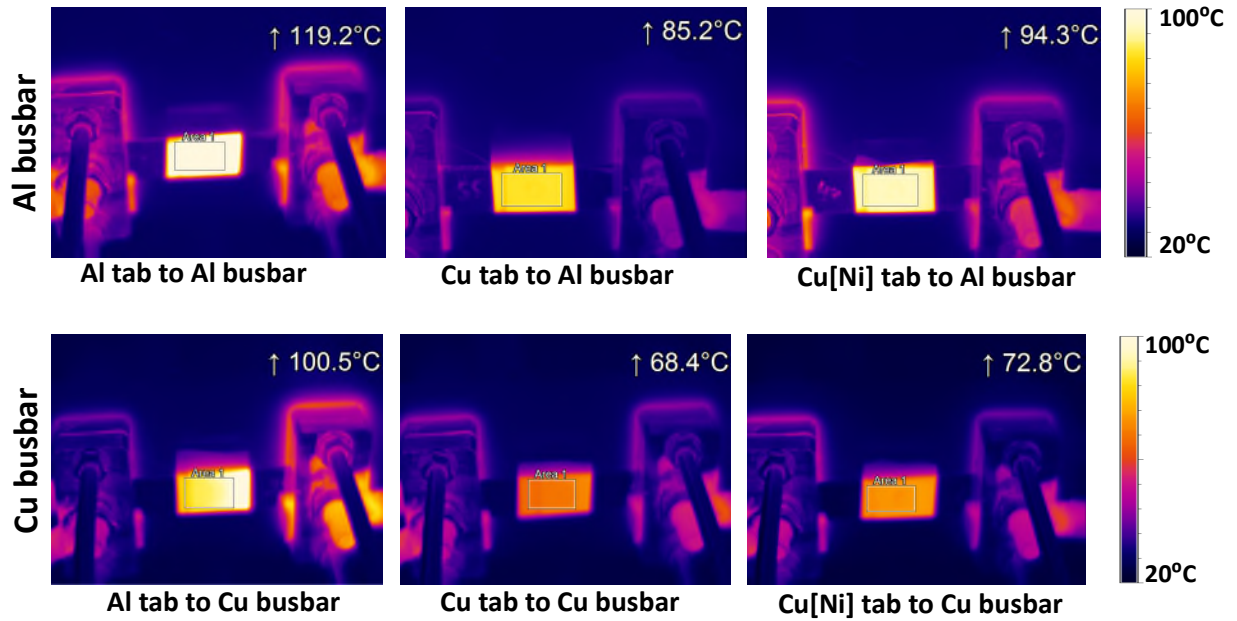
Fig. 27. IR thermal images as a result of current flow from various tabs to Al and Cu busbar joint at t= 180s at 200 A

Table 5. Rise in temperature at joints of laser welded various tabs to busbars materials

Tab materials	Temperature after 180s (°C)					
	I= 100 A		I= 150 A		I= 200 A	
	Busbar		Busbar		Busbar	
	Al	Cu	Al	Cu	Al	Cu
Al	51.9	41.3	79.6	70.1	119.2	100.5
Cu	42.2	34	68.9	46.5	85.2	68.4
Cu[Ni]	46	35.3	73	47.3	94.3	72.8
Ni	81.9	48	157.8	99	×	×

4. Conclusions

This paper presents an in-depth study on laser welding of the various tab (Al, Cu, Cu[Ni] and Ni) to busbar (Al and Cu) joints by conducting the mechanical, metallurgical, electrical and thermal characterisation. The results offer options for selecting the appropriate tab and busbar materials to achieve critical-to-quality criteria, such as low resistance, low-temperature rise and high joint strength for electrical interconnects used in battery manufacture. From the foregoing analysis and discussion, the following conclusions were drawn:

- This paper identified the parameters to achieve under-, good- and over-weld conditions for various tab-to-busbar combinations. For example, Al tab to Al busbar joints, laser powers of 300 W, 525 W and 675 W were required for under-, good and over-welds respectively.

- The weldment Ni tab and copper busbar provided maximum joint strength of about 1320 N followed by Ni tab and Al busbar joint of about 930 N. This is because the Ni tab to Cu busbar joint has no defects such as pores, cracks and undercut in case of good-weld parametric condition.

- The tensile strength obtained for the Cu tab to Al busbar joints were slightly more (about 7.5%) than the Al tab to Cu busbar joint as the IMCs generated at the weld interface of Al tab to Cu busbar joints were more than the Cu tab to Al busbar joints.

- Ni tab to Al or Cu busbar make good joints with respect to strength and microstructure but have poor electrical and thermal performance as well as being expensive. Whereas Cu and Cu[Ni] tabs provide good performance in terms of electrical and thermal characterisation.

- The lowest electrical resistance was obtained for the Cu tab to Cu busbar weld about R= 0.044 mΩ, 0.048 mΩ and 0.050 mΩ when a current of 100 A, 150 A and 200 A were applied for 180 s, respectively. This increase in resistance values was the result of the temperature rise due to resistive heating, therefore, with the rise of joint temperature, a positive feedback loop was observed.

- Cooper is traditionally used as busbar material. But the selection of Al busbar material over Cu busbar can reduce the weight and cost of the busbar used in the battery module by 75%. However, the Cu tab to Al busbar gave slightly higher (about 16-20%) resistance over the Cu tab to Cu busbar joint.

- The minimum rise in temperature at joint measured for the Cu tab to Cu busbar joints, 34°C for 100 A, 46.5°C for 150 A and 68.4°C for 200 A. However, in the case of Cu tab to Al busbar, 42.2°C for 100 A, 68.9°C for 150 A and 85.2°C for 200 A was measured which is about 23%, 47% and 25% higher respectively.

In conclusion, this paper outlined the feasibility of producing various tab-to-busbar joints using laser welding. These in-depth analyses of joint strength, IMCs, electrical contact resistance and temperature rise should enable/guide the battery manufacturers to design an efficient battery system by satisfying their critical-to-quality requirements. Furthermore, a detailed study correlating the electrical resistance to IMCs layer thickness and density is necessary and proposed as future work. In addition, XRD and EBSD analyses will be conducted for better understating of grain formation together with IMCs.

Reference

1. R. Faria, P. Moura, J. Delgado, AT de Almeida, 'A sustainability assessment of electric vehicles as a personal mobility system', Energy Conversion and Management 61 (2012) 19-30.

2. E. Union (2016) Comparative study on the differences between the EU and US legislation on emissions in the automotive sector.

3. P. Yang, J.-M. Tarascon, 'Towards systems materials engineering', Nature Materials 11 (2012) 560–563.

4. J.-M. Tarascon, M. Armand, 'Issues and challenges facing rechargeable lithium batteries', Nature 414 (2001) 359-367.

5. A. Das, D. Li, D. Williams, D. Greenwood, 'Joining technology for automotive battery systems manufacturing', World Electric Vehicle Journal 9 (2018) 1-13.

6. M.J. Brand, P.A. Schmidt, M.F. Zaeh, A. Jossen, 'Welding techniques for battery cells and resulting electrical contact resistances', Journal of Energy Storage 1 (2015) 7-14.

7. B. Mehlmann, A. Olowinsky, M. Thuilot, A. Giller, 'Spatially modulated laser beam micro welding of CuSn6 and nickel-plated DC04 steel for battery applications', Proceedings of 6th LAMP, Niigata, Japan (2013) 1–8.

8. M. Schweier, J.F. Heins, M.W. Haubold, M.F. Zaeh, 'Spatter formation in laser welding with beam oscillation', Physics Proceedings 41 (2013) 20–30.

9. B.L. Luan, G. Campbell, M. Gauthier, X.Y. Liu, I. Davidson, J. Nagata, M. Lepinay, F. Bernier, S. Argue, 'Surface modification and fabrication of Li-ion battery components for plug-in hybrid electric vehicle', ECS Transaction 25 (2010) 59–71.

10. S. Katayama, Introduction: fundamentals of laser welding, in: S. Katayama (Ed.), Handbook of laser welding technologies, Woodhead Publishing, Cambridge, UK, (2013) 3–17.

11. P. Schmidt, M. Schweier, M.F. Zaeh, 'Joining of lithium-ion batteries using laser beam welding: electrical losses of welded aluminium and copper joints', Proceeding of the 31th ICALEO, Anaheim, CA, (2012) 915–923.

12. T. Solchenbach, P. Plapper, W. Cai, 'Electrical performance of laser braze-welded aluminium–copper interconnects', Journal of Manufacturing Processes 16 (2014) 183–189.

13. J.A. Rayne, M.P. Shearer, C.L. Bauer, 'Investigation of interfacial reactions in thin film couples of aluminum and copper by measurement of low temperature contact resistance', Thin Solid Films 65 (1980) 381-391.

14. M. Kraetzsch, J. Standfuss, A. Klotzbach, J. Kaspar, B. Brenner, E. Beyer, 'Laser beam welding with high-frequency beam oscillation: Welding of dissimilar materials with brilliant Fibre lasers' PHYSICS Procedia 12 (2011) 142-149.

15. T.A. Mai, A.C. Spowage, 'Characterisation of dissimilar joints in laser welding of steel–kovar, copper–steel and copper–aluminium', Materials Science and Engineering A 374 (2004) 224–233.

16. P. Schmitz, J.B. Habedank, M.F. Zaeh, 'Spike laser welding for the electrical connection of cylindrical lithium-ion batteries', Journal of Laser Applications 30 (2018) 1-7.

17. G. Shannon, H. Chen, 'Laser welding of aluminium and copper for battery welding applications using a 500W single mode fibre laser', International Congress on Applications of Lasers & Electro-Optics, Congr. Proc. 102 (2009) 1015 – 1020.

18. P.A. Schmidt, T. Pauleser, M.F. Zaeh, 'Optimisation of weld seam configurations using a Genetic Algorithm, in 8th DET, Stuttgart, Germany, 2014.

19. D. R. Sigler and J. G. Schroth, 'Battery tab joint by reaction metallurgy', U.S. Patent 8 590 768 B2, Nov. 26, 2013.

20. L. Kirkpatrick, 'Aluminum Electrical Conductor Handbook', The Aluminum Association: Arlington, VA, USA, 1989.

21. A. Das, I. Butterworth, I. Masters, D. Williams, 'Evaluation of key geometrical and mechanical properties for remote laser welded AC-170PX Aluminium joints', Journal of Laser Micro/Nanoengg 14 (2019) 1-7.

22. P. A. Schmidt, M. Schweier, M. F. Zaeh, 'Joining of lithium-ion batteries using laser beam welding: Electrical losses of welded aluminum and copper joints', in International Congress on Applications of Lasers & Electro-Optics (ICALEO), Anaheim, 23–27 September 31 (2012) 915–923.

23. N. Kumar, M. Mukherjee, A. Bandyopadhyay, Comparative study of pulsed Nd:YAG laser welding of AISI 304 and 316 stainless steels, Optics & Laser Technology 88 (2017) 24-39.

24. M. Ishak, K. Yamasaki, K. Maekawa, Lap fillet welding of thin sheet AZ31 magnesium alloy with pulsed Nd:YAG laser, Journal of Solid Mechanics and Materials Engineering 3 (2009) 1045-1056.

25. E. Schrüfer, [Elektrische Messtechnik], Hanser, 221-223 (1990).

26. A. Das, T.R. Ashwin, A. Barai, Modelling and characterisation of ultrasonic joints for Li-ion batteries to evaluate the impact on electrical resistance and temperature raise, Journal of Energy Storage 22 (2019) 239-248.

27. A. Das, D. Li, D. Williams, D. Greenwood, 'Weldability and shear strength feasibility study for automotive electric vehicle battery tab interconnects', Journal of the Brazilian Society of Mechanical Sciences and Engineering 41 (2019) 54.

28. H. Tasalloti, P. Kah, J. Martikainen, Laser overlap welding of Zn-Coated steel on aluminium alloy for patchwork blank applications in the automotive industry, Reviews on Advanced Materials Science 40 (2015) 295–302.

29. K. Oussaid, A. El Ouafi, A. Chebak, Experimental investigation of laser welding process in overlap joint configuration, Chemistry of Materials 7 (2019) 16–31.

30. M. Masoumi, S.P.H. Marashi, M. Pouranvari, Metallurgical and mechanical characterization of laser spot welded low carbon steel sheets, Materials Technology 81 (2010) 1144–1150.

31. S. Meco, S. Ganguly, S. Williams, N. McPherson, Design of laser welding applied to T joints between steel and aluminium, Journal of Materials Processing Technology 268 (2019) 132–139.

32. J. Enz, V. Khomenko, S. Riekehr, V. Ventzke, N. Huber, N. Kashaev, Single-sided laser beam welding of adissimilar AA2024–AA7050 T-joint. Materials & Design 76 (2015) 110–116.

33. A. Das, A. Barai, I. Masters, D. Williams, 'Comparison of tab-to-busbar ultrasonic joints for electric vehicle Li-ion battery applications', World Electric Vehicle Journal 10 (2019) 55.

34. U.F. Shaikh, A. Das, A. Barai, I. Masters, 'Electro-Thermo-Mechanical Behaviours of Laser Joints for Electric Vehicle Battery Interconnects', In 2019 Electric Vehicles International Conference (EV) 2019 (pp. 1-6). IEEE.

35. J. Helm, I. Dietz von Bayer, A. Olowinsky, A. Gillner, 'Influence of the surface properties of the connector material on the reliable and reproducible contacting of battery cells with a laser beam welding process', Welding in the World 63 (2019) 1221–1228.

36. A. Das, T. Dale, I. Masters, D. Widanage, Feasibility of fillet edge weld using laser wobble technique, Procedia CIRP 95 (2020) 846-851.

37. P. Schmalen, P. Plapper, 'Evaluation of laser braze-welded dissimilar Al-Cu joints, 'Physics Procedia 83 (2016) 506-514.

38. N. Javani, I. Dincer, G.F. Naterer, G.L. Rohrauer, 'Modeling of passive thermal management for electric vehicle battery packs with PCM between cells', Applied Thermal Engineering 73 (2014) 307–316.

39. M. Abbasi, A.K. Taheri, M.T. Salehi, 'Growth rate of intermetallic compounds in Al/Cu bimetal produced by cold roll welding process', Journal of Alloys and Compounds 319 (2001) 233–241.

40. Z. Lei, X. Zhang, J. Liu, P. Li, 'Interfacial microstructure and reaction mechanism with various weld fillers on laser welding-brazing of Al/Cu lap joint', Journal of Manufacturing Processes 67 (2021) 226–240.

41. J. Huang, B. Yang, H. Chen, 'Thermodynamic optimisation of the Ni-Al-Y ternary system', Journal of Phase Equilibria and Diffusion 36 (2015) 357–365.

42. S. Chen, G. Yu, S. Li, J. Yang, S. Chen, 'Interfacial microstructures and mechanical property of Ni/Al dissimilar butt joint made by laser welding', Journal of Manufacturing Processes 50 (2020) 17-23.

43. H. Landolt, R. Bornstein, 'Phase equilibria, crystallographic and thermodynamic data of binary alloys' Springer-Verlag; 1993.

44. D. Zuo, S. Hu, J. Shen, Z. Xue, 'Intermediate layer characterization and fracture behavior of laser-welded copper/aluminum metal joints', Materials & Design 58 (2014) 357–62.

45. W.B Lee, K.S. Bang, S.B. Jung, 'Effects of intermetallic compound on the electrical and mechanical properties of friction welded Cu/Al bimetallic joints during annealing', Journal of Alloys & Compound 390 (2005) 212–9.

46. M. Braunovic, N. Alexandrov, 'Intermetallic compounds at aluminum-to-copper electrical interfaces: effect of temperature and electric current', Components Packaging & Manufacturing Technol Part A IEEE Trans 17 (1994) 78–85.

47. J.S. Seo, H.S. Jang, D.S. Park, 'Ultrasonic welding of Ni and Cu sheets', Materials & Manufacturing Processes 30 (2015) 1069–1073.

48. Z.L. Ni, J.J. Yang, F.X. Ye, 'Microstructure and mechanical properties of copper to nickel ultrasonic spot welds', Materials Science & Engineering A 796 (2020) 140207.

49. T.B. Massalski, 'Binary alloy phase diagrams', Materials Park: (OH): ASM International; 1990. p.183.

50. X. Zhao, Z. Shi, C. Deng, Y. Liu, X. Li, 'The effect of laser offset welding on microstructure and mechanical properties of 301L to TA2 with and without Cu intermediate Layer', Metals 10 (2020) 1138.

51. S. Yan, Y. Shi, 'Influence of Ni interlayer on microstructure and mechanical properties of laser welded joint of Al/Cu bimetal', Journal of Manufacturing Processes 59 (2020) 343–354.

52. L. Battezzati, 'Solid solutions in metals: from Hume-Rothery's rules to high entropy alloys', Acc. Sc. Torino. Quaderni, 30 (2019), 21-35.

53. W. Hume-Rothery, R.E. Smallman, C.W. Haworth, 'The structure of metals and alloys' The Institute of Metals, 1 Carlton House Terrace, London SW1Y 5DB, UK, 1988.

54. K.A. Gschneidner, P.R. Subramanian, In: Massalski TB, editor. Binary alloy phase diagrams. Metals Park (OH): ASM; 1986.

55. A. Shamsolhodaei, Q. Sun, X. Wang, B. Panton, H. Di, Y.N. Zhou, 'Effect of laser positioning on the microstructure and properties of NiTi-copper dissimilar laser welds', Journal of Materials Engineering and Performance 29 (2020) 849-857.

56. N. Kumar, A. Das, T. Dale, I. Masters, 'Laser wobble welding of fluid-based cooling channel joining for battery thermal management', Journal of Manufacturing Processes 67 (2021) 151-169.

57. Q. Zhang, R. C. Sekol, C. Zhang, Y. Li, B. E. Carlson, 'Joining lithium-ion battery tabs using solder-reinforced adhesive', Journal of Manufacturing Science and Engineering 141 (2019) 044502-7.

58. S. Hu, A.S. Haselhuhn, Y. Ma, Y. Li, B.E. Carlson, Z. Lin, 'Comparison of the resistance spot weldability of AA5754 and AA6022 aluminum to steels', Welding Journal 99 (2020) 224-38.

59. N. Kumar, M. Mukherjee, A. Bandyopadhyay, 'Study on laser welding of austenitic stainless steel by varying incident angle of pulsed laser beam', Optics & Laser Technology 94 (2017) 296-309.

60. O. Grong, Metallurgical modeling of welding, The Institute of Materials, Cambridge, Great Britain 1994.

61. D. Dehelean, V. Safta, R. Cojocaru, T. Halker, C. Ciuca, 'Monitoring the quality of friction stir welded joints by infrared thermography', Welding in the World, 52 (SPEC. ISS.) (2008) 621–626.

62. H. Wang, Y. Kawahito, R. Yoshida, Y. Nakashima, K. Shiokawa, 'Development of a high-power blue laser (445 nm) for material processing', Optics letters 42 (2017) 2251–2254.

63. M.S. Zediker, R.D. Fritz, M.J. Finuf, J. M. Pelaprat, 'Laser welding components for electric vehicles with a high-power blue laser system', Journal of Laser Applications 32 (2020) 022038.

64. A. Das, R. Fritz, M. Finuf, I. Masters, 'Blue laser welding of multi-layered AISI 316L stainless steel micro-foils', Optics and Laser Technology 132 (2020) 106498.

65. E. Boese, M. Finuf, M. Zediker, J.M. Pelaprat 'Blue lasers add power and brightness', 2020. https://www.industrial-lasers.com/welding/article/14173138/blue-lasers-add-power-and-brightness (accessed 11/08/2021).

66. A. Das, R. Beaumont, I. Masters, P. Haney, 'Macro-modelling of laser micro-joints for understanding joint strength in electric vehicle battery interconnects', Materials 14 (2021) 3552.

67. M.J. Brand, P.A. Schmidt, M.F. Zaeh, A. Jossen, 'Welding techniques for battery cells and resulting electrical contact resistances', Journal of Energy Storage 1 (2015) 7–14.

68. T. Solchenbach, P. Plapper, W. Cai, 'Electrical performance of laser braze-welded aluminum–copper interconnects', Journal of Manufacturing Processes 16 (2014) 183–189.

69. https://www.lme.com/ (Accessed 14-06-2021)

70. J. Carvill, 'Mechanical Engineer's Data Handbook' (1993) 102-145. https://doi.org/10.1016/B978-0-08-051135-1.50008-X.